EFFECTS OF FATIGUE IN THE ELASTIC REGIME ON
THE IMPACT PROPERTIES OF LOW CARBON
STEELS AND ITS RELATION TO FRACTURE TOUGHNESS

by

Robert William Canty and James F. Stubbins
Nuclear Engineering Program, UIUC

A Report of the

MATERIALS ENGINEERING - MECHANICAL BEHAVIOR

College of Engineering, University of Illinois at Urbana-Champaign

August 1984

EFFECTS OF FATIGUE IN THE ELASTIC REGIME ON THE IMPACT PROPERTIES OF LOW CARBON STEELS AND ITS RELATION TO FRACTURE TOUGHNESS

by

Robert William Canty and James F. Stubbins
Nuclear Engineering Program

Four low-carbon steels, one ferritic (SAE 1018) and three bainitic (A533B Cl I, Cl I HT, and Cl II) all with similar compositions, were fatigued in the elastic regime at a stress amplitude of ± 207 MPa (± 30 ksi) to 10^4 cycles. These fatigue conditions were in the elastic regime, well below the endurance limits for these steels. The SAE 1018 was fatigued at room temperature and 100°C and the A533B steels were fatigued at -100°C and room temperature. Following fatigue, instrumented impact tests were performed to determine changes in impact properties of each steel. The data obtained indicates that elastic fatigue causes an increase in ductility for SAE 1018, A533B Cl I, and A533B Cl I HT steels. Similar changes in the ductility were found regardless of the material temperature during fatiguing. The A533B Cl II steel retained its original impact qualities. Several correlations between Charpy V-Notch impact energy and fracture toughness were examined to make a qualitative assessment of these effects upon fracture toughness. The increase in ductility predicts a similar increase in fracture toughness.

A Report of the

FRACTURE CONTROL PROGRAM

College of Engineering, University of Illinois
Urbana, Illinois 61801
August 1984

ACKNOWLEDGEMENTS

TABLE OF CONTENTS

TABLE OF CONTENTS

v

LIST OF TABLES

LIST OF FIGURES

1.0 INTRODUCTION

In an effort to provide information for use in design applications, the fatigue and fracture properties of structural and load bearing steels have been under intensive investigation. A large body of data has accumulated and several theories have been proposed in an attempt to explain and predict the failure process. The instrumented charpy impact test provides such useful information as the ductile-brittle transition temperature (DBTT) and energy required for crack initiation and crack propagation. The DBTT reveals where failure by cleavage or brittle fracture occurs, a condition clearly to be avoided in engineering applications.

It has been established that steels possess an endurance limit such that fatigue at stress amplitudes below this level do not result in failure. The fatigue limit is well within the elastic regime and on the order of one third of the ultimate tensile stress. Prior investigations have shown that cycling below the fatigue limit can produce increased strength in some steels; materials subjected to increases in stress amplitude have longer lives than would be predicted for virgin material. Alterations in the steel's microstructure, such as the increase in dislocation density, are believed to occur during elastic cycling.

A set of correlations between Charpy V-Notch impact energy (CVN) and fracture toughness (K_{Ic}) have been developed to predict similar effects upon toughness. The present study explores the effects of fatigue in the elastic regime on the im-pact properties of four steels of similar

composition. The heat treatments are different, though, so that the initial microstructures and strengths are different. The structures represented are: a low to medium strength pearlitic steel (SAE 1018), two low to medium strength bainitic steels (A533B Class I and Class I Heat Treated) and a medium to high strength bainitic steel (A533B Class II). Correlations between CVN and K_{Ic} will subsequently be used to predict effects upon toughness.

2.0 LITERATURE SURVEY

2.1 Brittle Fracture Theories

Brittle cleavage fracture is commonly observed at low temperatures in iron and steel. At these temperatures the necessary normal stress for propagation of pre-existing cracks is exceeded by the material's yield stress. Of considerable importance in body centered cubic metals (BCC) is the high sensitivity to temperature exhibited by the yield strength. This behavior can be related to the temperature-sensitive Peierls-Nabarro stress contribution to yield strength, a large component at low temperature. Here, the thermal enhancement of dislocation motion is limited and the Peierls-Nabarro stress is large.[1] Eldin and Collins[2] and Wessel[3] generated data from tensile tests at various temperatures and found that the brittle fracture stress values at low temperature fell below the extrapolated yield stress curve.

Knott and Cottrell[4] observed that when mild steel breaks in a notch-brittle manner, the fracture is often ductile in the root of the notch but becomes brittle a short distance ahead of the notch. They proposed that a general yield stress is applied over the notched cross-section which, at low temperatures is more than three times greater than the required fracture stress. It was also noticed that the cleavage fracture mechanisms acted independently of temperature. They suggested that at low temperatures deformation occurred by twinning, that is cleavage crack nucleation at the junction of intersecting twins. An increase in temperature caused the twinning to be replaced by slip, however full cleavage fracture was still produced. Curry[5] agreed that

plastic flow preceeded cleavage and that yielding by slip or twinning was involved in the nucleation of cleavage fracture. Cottrell[6] also proposed that cracks could nucleate from two dislocations on intersecting slip planes by forming a sessile dislocation. A reduction of dislocation energy results and therefore crack nucleation is promoted. Here the cleavage fracture is propagation controlled and Eq. (2.1) identifies the cleavage fracture stress as

$$\sigma_f \geq \frac{2\mu\gamma}{K_y^s} d^{-1/2} \tag{2.1}$$

$$K_y^s = [\sigma_0 - \sigma_i(T)] d^{1/2} \tag{2.2}$$

where d is the grain size, γ the surface energy, μ the shear modulus, and K_y^s is the Hall-Petch yield strength parameter in Eq. 2.2 where σ_0 is the yield strength and $\sigma_i(T)$ is the friction stress or slip plane resistance to dislocation motion.[7] Eq. 2.1 suggests that σ_f is relatively insensitive to temperature and fine scale microstructure and that it is most sensitive to the grain size and K_y^s. Grain size is important since it is the obstacle to dislocation movement. This explains the effects of grain size and yielding parameters but neglects any other microstructural variables.

Lindley[8], among others[9] who realized size effects of precipitates, investigated an iron-carbon alloy with two different heat treatments used to vary the carbide morphology. The alloy was furnace cooled or air cooled to produce average carbide sizes of 5 to 6 μm and 1/2 to 1 μm, respectively, while each had similar ferrite grain sizes, twinning

characteristics, and were subjected to identical stress levels. He found that the presence of large carbide particles encouraged the formation of ferrite microcracks independent of deformation by slip or twinning. Cleavage cracks nucleate within brittle grain boundary carbide particles and may propagate into the ferrite if the local stresses and the applied stress are adequate. For a given plastic strain and testing temperature, more ferrite microcracks were observed in the furnace cooled material. The result indicates that thick carbide particles are more likely to produce ferrite cracks than thin particles. Oates[10] applied a superimposed hydrostatic tensile stress to notched specimens and found that this aided the growth of cleavage cracks across grains rather than through their boundaries. Below the notch, the local tensile stress becomes large enough to propagate cracks into the surrounding ferrite but grain size length microcracks were not observed in either notched bend or plain specimens following deformation. Note that the stress on a twin band is greater than that acting on a slip band for a given applied stress, therefore for a twin-induced crack failure is more likely to occur. These results reveal that growth is associated with precipitate size cracks in low carbon manganese steel.

Several reports relating effects of microstructure to fracture toughness and cleavage fracture stress in steels have been published by Curry and Knott[9,11,12]. Their model is useful in predicting the cleavage fracture toughness of steel containing spheriodal carbide particles from the carbide particle distribution. One must note that the plastic zone size is dependent upon temperature, being large for high temperatures and small, of the order of a few particle diameters, for

low temperatures. At these low temperatures, when the plastic zone radius r_p is small, a particle may have a pronounced effect upon the crack tip. Then, if r_p is small, this model can be modified to predict cleavage fracture toughness of any steel that fractures at cracked second phase particles by adjusting stresses corresponding to crack nuclei geometry. Experimental results show that the fracture toughness and cleavage fracture stress are functions of grain size. As the grain size decreases below about 30 µm, K_{Ic} values increase. Curry and Knott have developed a relation between carbide particle size, grain diameter, and the cleavage fracture stress which was originally proposed by Smith.[13] These effects can be seen in the following equation:

$$\left(\frac{C_o}{d}\right)\sigma_f^2 + \tau_e^2 \left\{1 + \frac{4}{\pi}\left(\frac{C_o}{d}\right)^{1/2}\frac{\tau_i}{\tau_e}\right\}^2 \geq \frac{4E\gamma_p}{\pi(1-\nu^2)d} \qquad (2.3)$$

where C_o is the thickness of the grain boundary carbide, E is Young's modulus, γ_p is the effective surface energy of ferrite, d is the slip band half-length, ν is Poisson's ratio, τ_i is the lattice friction shear stress, σ_f is the fracture stress, and τ_e is the effective shear stress. By assuming that the effective shear stress τ_e can be written as $K_y^S d^{-1/2}$ where d is now the grain size, the fracture criterion [Eq. 2.3] reduces to:

$$\sigma_f^2 + \left(\frac{K_y^S}{C_o}\right)^2 \left\{1 + \frac{4}{\pi}C_o^{1/2}\frac{\tau_i}{K_y^S}\right\}^{1/2} \geq \frac{4E\gamma_p}{(1-\nu^2)C_o} \qquad (2.4)$$

This predicts that the only microstructural parameter affecting the fracture stress is the carbide thickness, since K_y is a measure of the ease of unpinning or creating dislocations and is independent of grain size. Predictions made using Curry and Knott's model were seen to be in good agreement with experimental results for a variety of temperatures and steels.

This shows a general relationship between the ferrite grain size and the size of the largest carbide particle. Curry and Knott[11] assumed that spheriodal carbide particles crack and act as nuclei for cleavage crack propagation in a manner analogous to that of grain boundary carbides in normalized mild steels. The crack nucleus size distribution is proportional to the carbide particle size distribution. The crack nucleus would be penny-shaped in the case of a spheriodal particle, compared to the through the thickness nucleus produced in a grain boundary carbide film. The Griffith crack propagation criteria for a crack of half-length $r=C_0/2$ or radius r for these configurations are given in Eqs. 2.5 and 2.6 as

$$\sigma_f = \left(\frac{\pi E \gamma_p}{2(1-\nu^2)r} \right)^{1/2} \quad \text{penny-shaped} \tag{2.5}$$

$$\sigma_f = \left(\frac{2E\gamma_p}{\pi(1-\nu^2)r} \right)^{1/2} \quad \text{through thickness} \tag{2.6}$$

The change in shape from a through-thickness to a penny-shaped nucleus causes an increase $\pi/2$ in the fracture stress for a given nucleus size. The relation in Eq. 2.6 cannot be used directly in

conjunction with spheroidized steels because the stress intensity asso-
ciated with the change in crack nucleus shape is lower and also disloca-
tion pile ups will not occur across a grain diameter. Therefore the
cleavage fracture event may neglect any dislocation influences and can
be approximated as the Griffith crack propagation of penny-shaped
nuclei, with radii equal to those of the carbide particles. Fracture
then occurs when the largest cracked carbide particle is subjected to
enough tensile stress to satisfy the crack propagation energy balance.
Curry and Knott concluded that the representative coarsest-observed car-
bide particle thicknesses, the 95th percentile carbide radius, is a
reasonable estimate of the actual crack nucleus size which should be
treated as being penny-shaped.

Experimental results[7,14] have shown that an initially sharp crack
opens under increasing applied load prior to unstable extension. This
is important since the shape of the crack tip field remains constant as
the load or K increases while the real distance from the crack tip at a
specific value of applied tensile stress increases. Thus, the region of
material sampled by high tensile stress fields increases with load.
Ritchie, Knott, and Rice[15] suggested that the applied tensile stress
had to exceed the critical cleavage fracture stress over a critical
microstructural distance ℓ. In mild steel, unstable cleavage fracture
can result only if the tensile stress sufficient to initiate a crack at
a grain boundary carbide is also sufficient to propagate it through the
next grain boundary. The condition that the tensile stress applied
exceeds the critical tensile stress at a characteristic distance ℓ
yields values of the order of 2 to 4 grain diameters for this distance.

For a sharp crack however, the maximum stress intensification will be a fraction of this distance. This principle will be discussed more specifically in subsequent sections.

2.2 Ductile Fracture Theories

Ductile materials fracture by the nucleation, growth and coalescence of microvoids and is usually a consequence of slip. Hence shear stresses must be of primary importance. Knott[16] observed that the ductile fractures in quenched and tempered steels appeared to run from inclusion to inclusion, decohering the carbide/matrix interfaces, rather than having cracked the particles. He suggested that the decohesion was a direct effect of the applied tensile stress or local stresses produced by dislocation rings surrounding the particles. Stresses build up during plasticity and dislocations pile up around the carbides causing increasing local stresses at the interface as the plastic strain increases. Fracture occurs at a critical strain and increases the shear strain on other particles, in turn making them more likely to rupture at their interfaces. Further, a nucleation condition for particles of radius c ($<<$d) in a series of pile-ups of length d under an effective shear stress τ_{eff} is

$$\tau_{eff} = (\pi\mu\gamma/2(1-\nu)d)^{1/2} \cdot (c/d)^{1/2} \qquad (2.7a)$$

$$n\overline{b} = 2\gamma/\tau_{eff} \qquad (2.7b)$$

where μ is the shear modulus, ν is Poisson's ratio, γ is the interfacial energy, and n is the number of dislocations of Burgers vector b in the pile-up. In the case of the interfaces simply fracturing under the local applied tensile stress, more precise values of the interfacial cohesive strength are necessary.

The generation of dislocations during plastic deformation is a very chaotic process. In a model developed by Thomson and Sinclair[17], the two-dimensional creation of dislocations was analyzed and postulated as pairs of dislocations with opposite sign. The dislocations which act to shield the crack from the external stress are repelled from the crack by the crack stress intensity field. These dislocations have counterparts that act as anti-shielding dislocations which are attracted by the crack stress intensity field. In order for a net shielding effect on the crack, the anti-shielding dislocations must be absorbed by the crack surface. This yields the relation in Eq. 2.8 which relates the total Burgers vector to the crack opening displacement

$$COD = \sum_j (b_j)_y \qquad (2.8)$$

This led Thomson and Sinclair to the correlation between crack opening displacement and the overall toughness because a high screening "charge" of total Burgers vector is related to higher toughness. They developed this model because a moving crack could not be sufficiently analyzed since the region very close around the crack is loaded up, then plastically deformed, and finally unloaded as the crack moves past.

In an analysis of an aluminum alloy containing impurity particles, Tanaka, Pampillo, and Low[18] noticed a boundary between fatigue crack and dimpled rupture regions of the fracture surface. This transition area or stretched-zone they believe was produced during blunting of the tip and perhaps some stable crack growth. The size of the stretched zone seemed to be on the order of $G_{Ic}/4\sigma_y$, where G_{Ic} is the critical

crack extension force and σ_y the yield stress. Assuming that the uniaxial yield strength is doubled under plane strain conditions, then $G_{Ic}/2\sigma_y$ can be used as the COD at instability and the radius of the crack tip prior to instability is of the order of 1/2 to 1 times the COD in size. While the stretched zone formed, voids were believed to nucleate around particles and then coalesce. The fracture process may, therefore, depend upon the distance between particles through which the matrix must fail.

It is noteworthy to point out that ductile fracture must take into account that a number of processes are involved and each differs from one material to another. Therefore, a variety of fracture criteria is needed to characterize the different stages. Voids for example may be created in several ways such as, fracture of secondary particles, decoherence of articles from the matrix, or from dislocation interactions. These holes may then grow by plastic flow, fracture along grain boundaries, or sliding off. At least 14 modes for initiation of fracture are specified by McClintock.[19] These modes may occur separately or two or more may exist at once. He also considers several different modes of propagation including repeated nucleation of cracks. Here the fracture criterion would be satisfied at some point inside the logarithmic spiral region growing ahead of the crack tip due to crack blunting. Fracture occurs immediately and a sharp notch is produced which again blunts until another logarithmic spiral region moves ahead, and so on.

Precise measurement of fracture surfaces is difficult to achieve especially after plastic flow has occurred. Beachem[20] has studied fracture surfaces formed by microvoid coalescence and has found that

these surfaces seldom have identical dimple mates. This occurs because the surfaces are deformed differently during separation and after they separate. The differences in shapes can be used to reconstruct crack tip deformation directions and determine crack tip stress directions and magnitudes since differences in degree of plastic flow indicate similar differences in degree of stress. Also it is postulated that the direction of principle plastic flow is the direction of principle tensile stress. The use of precision matching techniques allowed Beachem to determine 14 probable dimple shapes related to the three "pure" fracture modes I, II, and III.

2.3 Fracture Toughness-CVN Correlations

Brittle fracture is clearly a mode of fracture that must be avoided. Impact testing provides a means of determining the ductile brittle transition temperature (DBTT), where below the DBTT the energy absorbed by a specimen in fracture is very small and nominal stresses well below the yield strength may cause fracture at the yield strength. strength. Above the DBTT the energy absorbed in fracture is large and the nominal stresses must exceed the yield strength to produce fracture. Although linear elastic fracture mechanics can be used to produce quantitative results relating fracture toughness to nominal stress and flaw size, the Charpy test sample method holds certain advantages, such as ease of preparation, relative simplicity, low cost, and small specimen size. This suggests the need for a relation between fracture toughness and the measured toughness from the Charpy V-notch (CVN) test. An attempt to correlate the mag-

nitude of the CVN energy absorption with the magnitude of the respective K_{Ic} value at the corresponding temperatures was made by Barsom and Rolfe[21] since they saw that at the onset of the temperature transition for dynamic K_{Ic}, data occurs at approximately the same temperatures as the onset of temperature transition for impact CVN data. They developed relations in two separate regions, the upper-shelf and the transition-temperature region. The upper-shelf K_{Ic}-CVN correlation in Equation 2.9 was developed empirically from results obtained on several steels.

$$\frac{K_{Ic}}{\sigma_y}^2 = \frac{5}{\sigma_y} \left(CVN - \frac{\sigma_4}{20} \right) \quad \left(in., \frac{ft \cdot lb}{KSI} \right) \tag{2.9}$$

The transition-temperature K_{Ic}-CVN correlations was also developed empirically and was found to be

$$\frac{K_{Ic}^2}{E} = 2(CVN)^{3/2} \tag{2.10}$$

where K_{Ic} is in KSI$\sqrt{in}$ and CVN is in ft·lbs. These results cannot be theoretically justified because of differences in loading rate and notch sharpness. For these reasons Barsom and Rolfe also made a comparison of slow-bend and impact CVN test results to learn the effects of varied loading rates. Failure in structures may occur with a relatively high loading rate however it is not clear that the loading rate would ever become high except during an accident. Odette and Lucas[7] studied several models that correlated fracture toughness to Charpy impact energy. Their conclusions suggest that such correlations exist and data may be used to guide development efforts but the results should not be the only criterion. They found that the most conservative correla-

tion was determined by Sailors and Corten[22]. In their study a series of guidelines for evaluating and selecting the data for a correlation of K_{Ic} with CVN was used. Charpy data at one temperature frequently exhibits a large scatter in data points, therefore, attention must be paid to the lower boundary of the energy band. Also at low temperatures the energy values are less reliable due to inertial effects. Using these guidelines, the empirical correlation found between K_{Ic} and CVN was

$$K_{Ic} = 15.5(CVN)^{0.5} \quad \text{or} \tag{2.11a}$$

$$\frac{K_{Ic}^2}{E} = 8 \ CVN \tag{2.11b}$$

where $K_{Ic}2/E$ is in psi/in, $E=30\times10^3$ ksi, and CVN in ft·lbs. Comparison of K_{Ic} estimated from Charpy data and the measured values for K_{Ic} showed good agreement when predicted from Eq. 2.11a. The correlation can be unconservative or over-conservative and emphasizes that no single correlation between K_{Ic} and CVN accurately fits all data. They believe that correlations can be devised to fit certain classes of steels, such as metallurgically uniform thick pressure vessel steel plate, but they are conservative. A similar empirical relationship was found between the dynamic fracture toughness K_{Id} and CVN. By fitting data using the method of least squares on log-log coordinates the correlation was found to be

$$K_{Id} = 15.873(CVN)^{0.375} \tag{2.12}$$

where K_{Id} is in units of ksi$\sqrt{in}$ and CVN is in ft·lbs.

The rate of loading shows a marked influence on the relationship between K_{Ic} and CVN. The difference between exponent in Eqs. 2.11 and 2.12 causes K_{Id} values to be lower than K_{Ic} values. In general Eq. 2.12 was found to be good for either static or dynamic testing when compared with the results of Barsom and Rolfe[21]. To further help determine the effects of temperature on fracture toughness an attempt to estimate K_{Id} from DBTT was made. The relation

$$\frac{\sigma_{yd}}{K_{Id}} = \frac{T' - NDT}{0.634 \, S_\perp} \tag{2.13}$$

where NDT is the nil ductility temperature, T' and $S_\perp$ are material constants, and σ_{yd} is the dynamic yield strength shows that by shifting K_{Id}/σ_{yd} with temperature, K_{Id} and σ_y shift the same temperature increment. This provides a direct comparison between the temperature increment, ΔT, and the change in fracture toughness.

An investigation carried out by Koppenaal[23] related K_{Id} to total energy per unit area for fracture W/A and energy per unit area to reach maximum load W_m/A. The empirical relationship

$$\frac{K_{Id}^2}{E} = \frac{1}{(1-\nu^2)} \, \frac{W_m}{A} \tag{2.14}$$

$$\frac{W_m}{A} \simeq \frac{1}{2} \frac{W}{A} \tag{2.15}$$

predicts identical static behavior and dynamic behavior for low values of K_{Id}. Each model discussed shows that no precise relation exists for all materials, however, empirical results suggest that correlations may be valid for certain classes of materials.

Hahn and Rosenfield[24] considered four basic factors that contribute to the fracture toughness of metals. These are the character and amount of plastic flow at the crack tip in plane strain or plane stress, the peak strain generated and the critical strain for rupture. They are used because the concepts of plane strain and plane stress are associated with the lower and upper limit of toughness. An important difference between them is that the same crack-tip displacement produces a smaller strain concentration under plane stress than under plane strain. Eqs. 2.16 relate the zone size ρ and crack tip displacement ν to fracture toughness.

$$\rho \text{ (plane strain)} \approx \frac{\pi}{16} \left(\frac{K_{Ic}}{\sigma_y} \right)^2 \tag{2.16a}$$

$$\rho \text{ (plane stress)} \approx \frac{\pi}{8} \left(\frac{K_c}{\sigma_y} \right)^2 \tag{2.16b}$$

$$\nu_c \text{(plane strain)} \sim \frac{Y}{4E} \left(\frac{K_{Ic}}{\sigma_y} \right)^2 \tag{2.16c}$$

$$\nu_c \text{(plane stress)} \approx \frac{Y}{2E} \left(\frac{K_c}{\sigma_y} \right)^2 \tag{2.16d}$$

These equations are reasonably good for quantitative descriptions however are based on materials showing little or no strain hardening and must be modified for strain hardening materials. Displacement values are only useful when converted to local plastic strain. This model suggests that overlapping regions of shear have a finite width ℓ which is related to strain hardening. This gives the results

plane strain $\epsilon_c \approx \dfrac{Y}{2\ell_n E} \left(\dfrac{K_{Ic}}{\sigma_y} \right)^2$ (2.17a)

plane stress $\epsilon_c \approx \dfrac{2Y}{\ell_{n,t} E} \left(\dfrac{K_c}{\sigma_y} \right)^2$ (2.17b)

for ϵ_c, the peak crack tip strain, which are good first approximations. Although complications arise due to directionality of properties and the dependence of the critical true strain $\overline{\epsilon^*}$ on triaxial stress states, Hahn and Rosenfield made the approximations:

$\overline{\epsilon^*}$ (ahead of a crack) $\propto \overline{\epsilon^*}$ (tension test) (2.18a)

$\overline{\epsilon^*}$ (plane strain zone) $\sim 1/3\ \overline{\epsilon^*}$ (tension test) (2.18b)

$\overline{\epsilon^*}$ (plane stress zone) $\sim 1/2\ \overline{\epsilon^*}$ (tension test) (2.18c)

and combined Eqs. 2.18b and 2.18c with Eqs. 2.17a and 2.17b respectively to formulate:

$K_{Ic} \approx \sqrt{2/3\ EY\ \ell_n^*\, \overline{\epsilon^*}}$ (2.19a)

$K_c \approx \sqrt{1/4\ EY\ \ell_{n,t}^*\, \overline{\epsilon^*}}$ (2.19b)

where ℓ_n^* and ℓ_{nt}^* are the values of ℓ at the onset of cracking. Further a correlation between ℓ_n^* and n, the strain hardening exponent, was obtained from data and is given as:

$\ell_n^* \approx n^2\ \ell$(inches) (2.20)

Next, by substituting n^2 for ℓ_n^* in Eq. 19a,

$$K_{Ic} \approx \sqrt{2/3 \; EY \; \overline{\epsilon}^* \; n^2}$$

(2.21)

This suggests that K_{Ic} is proportional to n and points toward the conclusion that strain hardening has a great influence on crack extension resistance. This theory is supported by a number of investigations (25,26,27).

In a more recent investigation by Hahn and Rosenfield[28], metallurgical factors affecting fracture toughness in aluminum alloys were discussed. By relating toughness with resistance to ductile or fibrous crack extension involving second phase particles, the significant metallurgical factors appeared to be: 1) the distribution of the particles that crack, 2) the resistance of the particles and their interfaces to cleavage and decohesion, 3) the local strain concentrations which accelerate the linking-up process of void nuclei, and 4) the grain size when the linking-up process involves the grain boundaries. Large, intermediate, and small inclusion size must also be considered.

The effects of inclusions on crack propagation is easily seen in their presence within voids on the fracture surface. Large inclusions were observed to crack by cleaving just after plastic flow began and did so because of the high stresses generated around them in the deformed matrix. The connection between the inclusion particles and the fracture toughness involves the plastic zone that surrounds the crack tip. In the small zone adjacent to the crack tip, large strains are produced by the large interface stresses that occur. Calculations by Rice and

Johnson[29], Hutchinson[30], and by Levy et al.(31) show that plastic strains of order $\varepsilon_p \sim 1$ are generated in the region of large plastic deformation, which extends a distance similar to the crack opening displacement δ, and is:

$$\delta \approx \frac{.5K^2}{E\sigma_y} \tag{2.22}$$

At the beginning of crack extension $\delta = \delta^*$ and $K = K_{Ic}$ and the deformed region is about the size of the ligaments between cracked particles:

$$\lambda_c \approx \delta^* \tag{2.23}$$

where λ_c is the spacing of cracked particles. Therefore the relationship between δ^* and K_{Ic} using Eq. 2.22 is:

$$K_{Ic} \approx \left[2\sigma_y \ E \ \frac{\pi}{6}^{1/3} \ D \right]^{1/2} \ f_c^{-1/6} \tag{2.24}$$

This relation has been restated in terms of the volume fraction f_c, and diameter D of cracked particles. It is reasonable to assume that all of the particles in the vicinity of the crack rupture or decohere because of the plastic strain that precedes the crack tip. Thus, f_c can be replaced by f_v, the total volume fraction of second phase particles. This relation was shown to predict values of the right order of magnitude by Birkle, Wei, and Pellisier,[32] Mulherm and Rosenthal,[33] Low and coworkers,[34] and others[35,36] however $K_{Ic}/\sqrt{E\sigma_y}$ values decrease with increasing yield strength at constant volume fraction contrary to Eq. 2.24. Also calculated values of δ^* do not always correlate with

cracked particle spacing. This may be the result of a third process, the premature rupture of material between voids due to local plastic instabilities.

There is some agreement that intermediate particles rupture or decohere and are responsible for small, closely spaced dimples. Thomson and Levy[37] gathered data that indicated the dimple spacing is often larger than the particle spacing, signifying that voids formed at only a fraction of the intermediate particles in the path of the crack. This suggests that the intermediate particles are more resistant to cracking or decohesion than the larger inclusions. The fine precipitate particles were observed to have at least two effects. They increase the resistance to deformation, reducing the crack opening displacement and enhancing toughness, while hardening the material. There is also a tendency for slip localization in the form of superbands and large slip offsets.

R. Roberts and C. Newton[38] collected several K_{Ic}-CVN correlations for the upper-shelf region and transition region. As has been emphasized already, the CVN-K_{Ic} correlations of each researcher is most likely to be valid for only the group of materials that each respectively studied. However, Roberts and Newton developed a very conservative relation, using their collection of studies:

$$\left(\frac{K_{Ic}}{\sigma_{ys}}\right)^2 = 0.52\left(\frac{CVN}{\sigma_{ys}} - .02\right) \quad (m, \ J/MPa) \tag{2.25a}$$

$$\text{or} \quad \left(\frac{K_{Ic}}{\sigma_{ys}}\right)^2 = 4.0\left(\frac{CVN}{\sigma_{ys}} - .01\right) \quad \left(in, \ \frac{ft \cdot lbs}{ksi}\right) \tag{2.25b}$$

which is valid for the upper shelf region. The actual K_{Ic} value for the material can be significantly greater, but for most it is very unlikely that the value will be less than that calculated by the equation. Another conservative relationship for the transition region was developed. They suggest the following relationship, for dynamic loading conditions, between K_{Id} and CVN.

$$K_{Id} = 22.5 \ (CVN)^{0.17} \quad (MPa\sqrt{m}, J) \tag{2.26a}$$

$$K_{Id} = 21.6 \ (CVN)^{0.17} \quad (Ksi\sqrt{in}, \ ft \cdot lb) \tag{2.26b}$$

The CVN value is between 7J (5ft·lbs) and the average of the upper and lower shelf values. Again the values of K_{Id} generated from these quations will most likely be lower than the actual K_{Id} and are highly unlikely to be greater. These K_{Id} values may be related to K_{Ic} using the dynamic fracture toughness correlation and temperature shift method of J. M. Barsom[39].

$$K_{Ic}(T-\Delta T_s) = K_{Id}(T) \tag{2.27}$$

where

$$\frac{K_{Id}^2}{E} = 0.64 \ CVN \quad (KPa\text{-}m, J) \tag{2.28}$$

$$\Delta T_s = 119 - 0.12\sigma_{ys} \quad (C°, MPa) \qquad 250 < \sigma_{ys} < 990 \ MPa \tag{2.29a}$$

$$\Delta T_s = 0 \qquad\qquad\qquad\qquad \sigma_{ys} > 990 \ MPa \tag{2.29b}$$

or

$$\frac{K_{Id}^2}{E} = 5 \ CVN \quad (psi\text{-}in, \ ft \cdot lb) \tag{2.30}$$

$$\Delta T_s = 215 - 1.5 \ \sigma_{ys} (F°, ksi) \qquad 36 < \sigma_{ys} < 140 \ ksi \tag{2.31a}$$

$$\Delta T = 0 \ \sigma_{ys} > 140 \ ksi \tag{2.31b}$$

The empirical nature of the correlations may cause a considerable difference between predicted and actual fracture toughness values but the general trend may be evaluated. K_{Ic} and K_{Id} curves are of similar shape and increase rapidly as temperature increases and the knowledge of where the sharp increase occurs provides a rough estimate which may be useful in design. Figure 2.1 shows a comparison of simple K_{Ic} relationships with two step correlations using the A533B data of Hawthorne and Mager[40]. A two step correlation uses a corresponding temperature shift with a simple correlation. The simple correlations are more conservative than the two step correlations which is an advantage, however, they may not be at the correct temperature range. A multiple step correlation has the advantage of allowing for strain rate effects and is preferred for static loading conditions.

2.4 K_{Ic}-CVN Correlation Limitations

Ritchie[41] has investigated the effects of austenitization temperature and notch acuity on the fracture toughness of AISI 4340 steel. This ultra high strength steel is typically austenitized at low temperature (870°C) to produce a fine prior austenite grain structure. More recently higher austenitization temperatures (870-1200°C) have been employed to increase the toughness without losses in strength. The toughness has been nearly doubled however the CVN energy has not exhibited like increases. The CVN energy has even concurrently decreased with the increase in toughness. To explain this paradox one must examine the microstructural fracture process for both sharp cracks (i.e. fracture toughness specimen) and rounded notches (i.e. CVN specimen). In
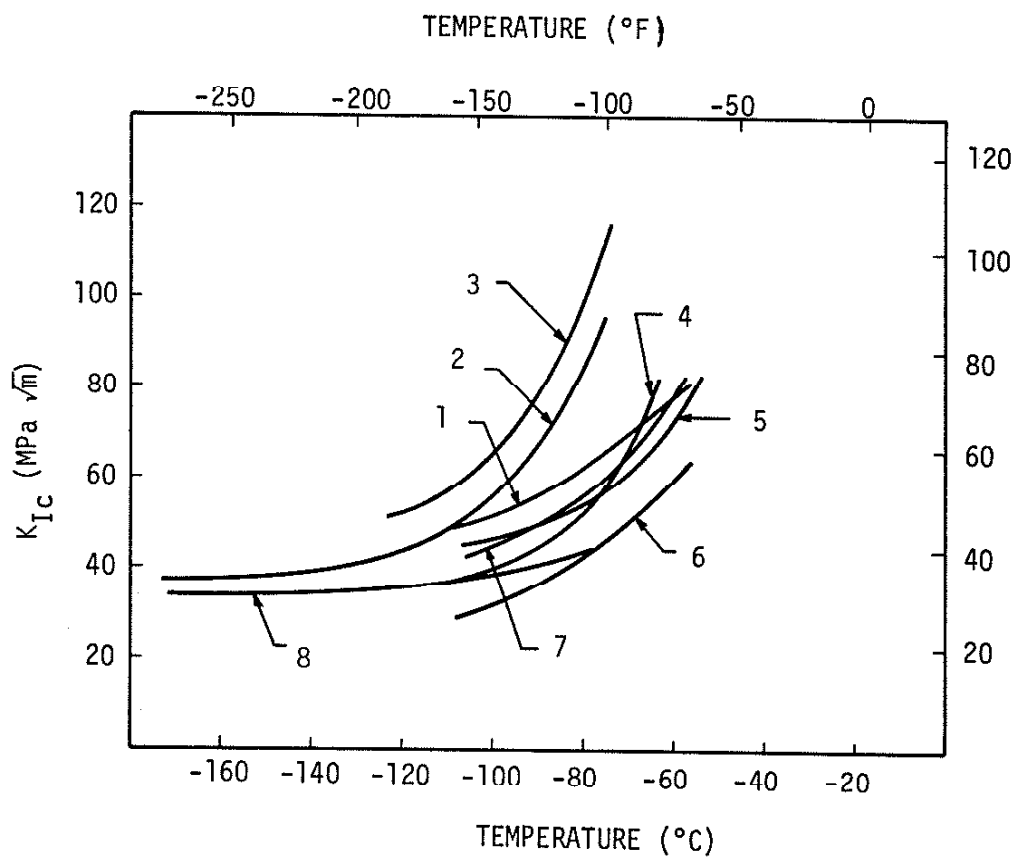
TEMPERATURE (°F)

Figure 2.1   Comparison of multiple step and simple K_{Ic}-CVN correlations using data for A533B steel: 1-Thorby-Ferguson, 2-Barsom-Rolfe two-step, 3-Marandet-Sanz two-step, 4-Barsom-Rolfe simple, 5-Sailors-Corten, 6-Lehigh lower bound simple, 7-Thorby-Ferguson two step, 8-Lehigh lower bound two step after Hawthorne and Mager[40].

order for the critical fracture event to occur ahead of a sharp crack, the fracture stress σ_F must be exceeded over a characteristic distance ℓ, which is on the order of one grain diameter. The maximum tensile stress σ_{yy}^{max} occurs at a distance less than the characteristic distance which is very close to the crack tip. The maximum tensile stress ahead of a rounded notch occurs at or just before the plastic-elastic interface. This distance is much greater when compared with the characteristic distance.

With this in mind, examination of the effects of raising the austenitization temperature shows a decrease in the critical fracture stress σ_F, and an increase in the limiting notch root radius or characteristic distance. The decrease in σ_F has been associated with impurity-induced grain boundary embrittlement caused by the high temperature austenitizing treatment, whereas the increase in characteristic distance has been associated with an order of magnitude increase in the prior austenite grain size and carbide spacings.[42]

Therefore, ahead of a rounded notch, the maximum tensile stress will be situated close to the plastic-elastic interface which is well beyond the characteristic distance. Here the toughness is controlled by the fracture stress σ_F. An increase in austenitizing temperature will decrease σ_F and thereby reduce the toughness. In the case of a sharp crack, σ_{yy} must exceed the fracture stress over the characteristic distance, which increases following an increase in austenitization temperature. Evidently the increase in σ_{yy} must overcompensate for the reduction in σ_F, resulting in a net increase in toughness.(See Figure 2.2)
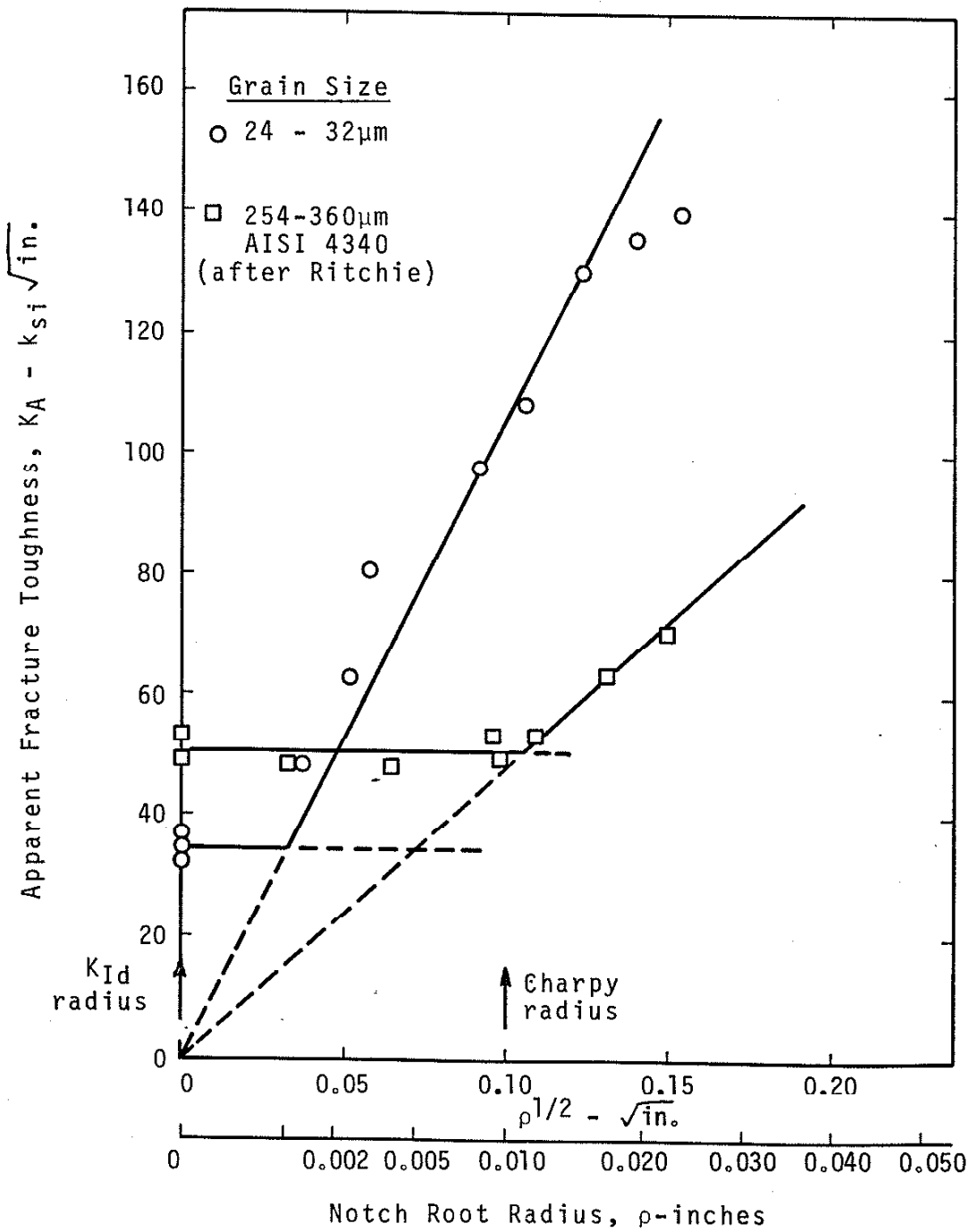
Figure 2.2 Apparent fracture toughness versus notch acuity
for AISI 4340 steel after Ritchie (41).

The above analysis is only valid for stress-controlled fracture mechanisms, however, similar behavior is observed for strain-controlled fracture on the upper shelf level. The notch radius is of paramount importance in determining the toughness as the microstructure is varied. Another characteristic distance is suggested, one that must require the critical strain be exceeded. This is a measure of the minimum amount of material ahead of the notch tip in which failure initiation mechanisms may operate. In the case of microvoid coalescence around inclusions, the distance is probably related to the particle spacing or distribution.

To analyze the effects of increasing the austenitization temperature, the effect upon the critical fracture strain must be considered. As the austenitization temperature is raised for as-quenched 4340 a marked reduction in ductility is observed. A reduction in "rounded notch" toughness can be related to this decrease in ductility where microstructurally the strain concentrations are greater at the boundaries between coarser martensite packets.(43) Now, ahead of a "sharp crack" the toughness increases. To explain this Ritchie analyzed the critically stressed volume and concluded that since the minimum amount of material with which the critical value of strain must be exceeded increased (i.e. characteristic distance), the toughness also increased. The effect of raising the austenitizing temperature also is to increase the distances between void-initiating particles caused by dissolution of carbides at high temperatures.(44)

It is concluded that evaluation of material toughness should include an assessment of resistance to fracture ahead of both sharp and rounded notches, especially if materials processing design procedures are changed.

2.5 Relation to Present Research

The purpose of the present work is to investigate the effects of fatigue in the elastic regime on the impact properties of low carbon steels. There is evidence that possible increases in ductility may result which are beneficial in some industrial applications. The low carbon steels are A533B Class I, I HT, and II, and SAE 1018, a plain carbon steel used in heavy industry. All types of steel have similar chemical compositions with carbon content at about .19 weight %. The A533B steels possess medium to high strength and high toughness whereas the SAE 1018 is low to medium strength and toughness.

The correlations provide a means for predicting toughness values of prefatigued steel. Despite their empirical and conservative nature, their results determine the general trends to be expected following fatigue at low stress amplitudes. It is anticipated that the steels will show dissimilar results when subjected to fatigue testing and subsequent impact testing due to differences in microstructural parameters such as grain size and carbide distribution.

3.0 EXPERIMENTAL PROCEDURE

3.1 Materials

Four low carbon steels were used in this investigation, SAE 1018, a plain low carbon steel, A533B Class I as-received, A533B Class I HT (heat treated), and A533B Class II as received. The chemical compositions by weight percentage are given in Table 3.1. The A533B Class I HT steel was cut from a newly manufactured pressure vessel, which received a post-weld stress relief heat treatment, and came in the form of 60.325mm (2 3/8") plate. The A533B Class I and SAE 1018 steels were 25.4mm (1") thick plates whereas the A533B Class I was 50.8mm (2") thick plate. All fatigue specimens were cut with the normal stress axis parallel to the rolling direction. Three specimen designs were necessary due to length and thickness differences in the stock (see Figure 3.1).

3.2 Mechanical Testing Techniques

An MTS hydraulic test machine with reversible load design and a maximum loading capacity of 2.67 MN(600 kip) was used for fatigue cycling. The grip requirement of 6" per end of each specimen made it necessary to weld small blocks of similar steel to the ends of the specimens. This technique was used to facilitate the testing of larger specimens.

The fatigue tests were run in the fully reversed load-controlled mode. Specimens received 10^4 cycles at a stress amplitude of $\pm$ 207 MPa ($\pm$30 ksi) with a frequency of 3.5 Hz and zero mean stress. Each material

Table 3.1 Chemical Compositions of A533B and SAE 1018 Steels

CHEMICAL COMPOSITIONS (weight %)

Element	A533B Class I*	A533B Class I HT**	A533B Class II***	SAE 1018****
Carbon	0.19	0.19	0.193	0.18
Manganese	1.30	1.32	1.340	0.82
Phosphorus	0.009	0.013	0.008	0.012
Sulfur	0.006	0.013	0.003	0.016
Silicon	0.23	0.22	0.210	<.05
Molybdenum	0.50	0.54	0.500	<.03
Nickel	0.53	<.05	0.600	<.05
Copper	0.13	0.12	0.070	0.24
Chromium	0.15	<.05		<.05
Aluminum	0.049			

   * Supplied by Lukens Steel Company
  ** Donated by Combusion Engineering, Inc.
 *** Supplied by Creusot-Loire, France
**** Supplied by U.S. Steel, Inc.
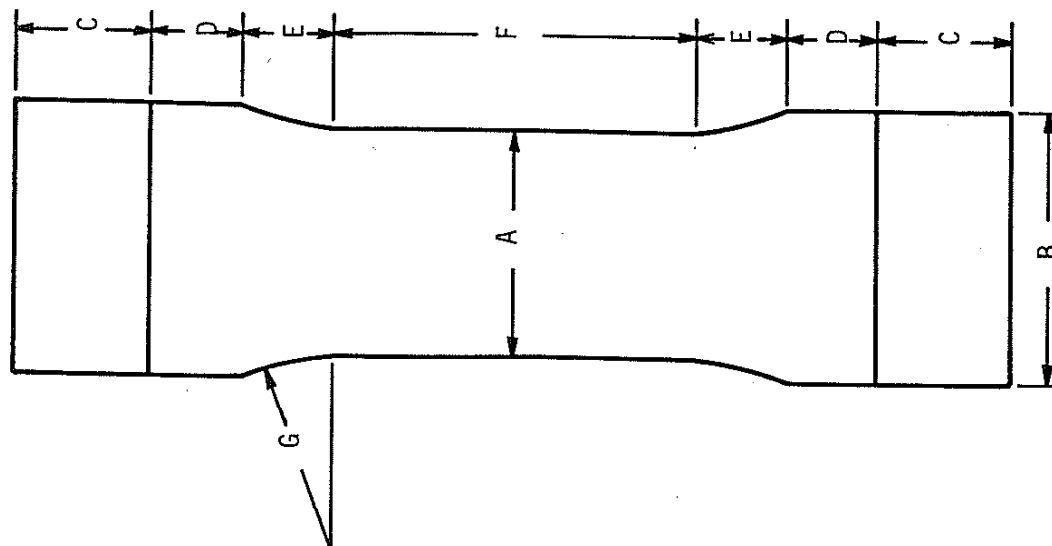
Dimension (cm)	SAE 1018	A533B I	A533B I HT	A533B II
A(cm)	15.24	7.62	6.03	7.62
B(cm)	16.51	8.89	7.30	8.89
C(cm)	11.81	7.37	12.35	7.37
D(cm)	3.43	7.87	2.89	7.87
E(cm)	4.19	3.56	3.302	3.56
F(cm)	45.72	22.86	18.1	22.86
G(cm)	13.97	10.16	8.89	10.16
thickness (cm)	2.54	5.08	6.03	2.54
Quantity	2	2	2	4

Figure 3.1 Dimensions of axial fatigue and IPST specimens.

has a yield stress upwards of 344 MPa (50 ksi) so the fatigue was constantly in the fully elastic regime (i.e. $\sigma = \epsilon E$). The SAE 1018 was fatigued at room temperature (RT) and at +100°C (FT). Fatigue tests of the A533B steels were performed at RT and at approximately -100°C(LT). The temperature choices allowed observation of the effects of fatigue under both brittle and ductile conditions for each steel.

Heating and cooling tanks were constructed for the SAE 1018 and A533B steels respectively. Both sets of tanks were made from copper sheet bent into L-shaped buckets which were then soldered. The L-shape provided a good fit around the specimens. To ensure good conductivity between specimen and tank, a highly viscous heat sink compound* was evenly spread across the sides of both the specimens and tanks. The cooling tanks were insulated with 1" of styrofoam sheeting enclosed by 1/4" plywood sheeting. The heating tanks were not insulated due to direct heating of the copper with ordinary Corning heating plates. The +100°C temperature was achieved by boiling water whereas the low temperature tests were maintained by using liquid nitrogen as coolant. The surface temperature of both sides of each specimen was monitored by affixing thermocouples along the gauge length with plastic tape. (see Figure 3.2).

An incremental plastic strain test (IPST) was performed on the A533B Class II steel which was controlled manually, allowing increments of 0.1% following stable hysteresis loops at the preceeding strain level. This procedure was repeated during unloading. The stress-strain history was recorded on an x-y plotter.

*Manufactured by Dow Corning

Fatigue Axis

Thermocouple
Placement

Heat
Conducting
Compound

Insulated
Cooling
Heating
Tank

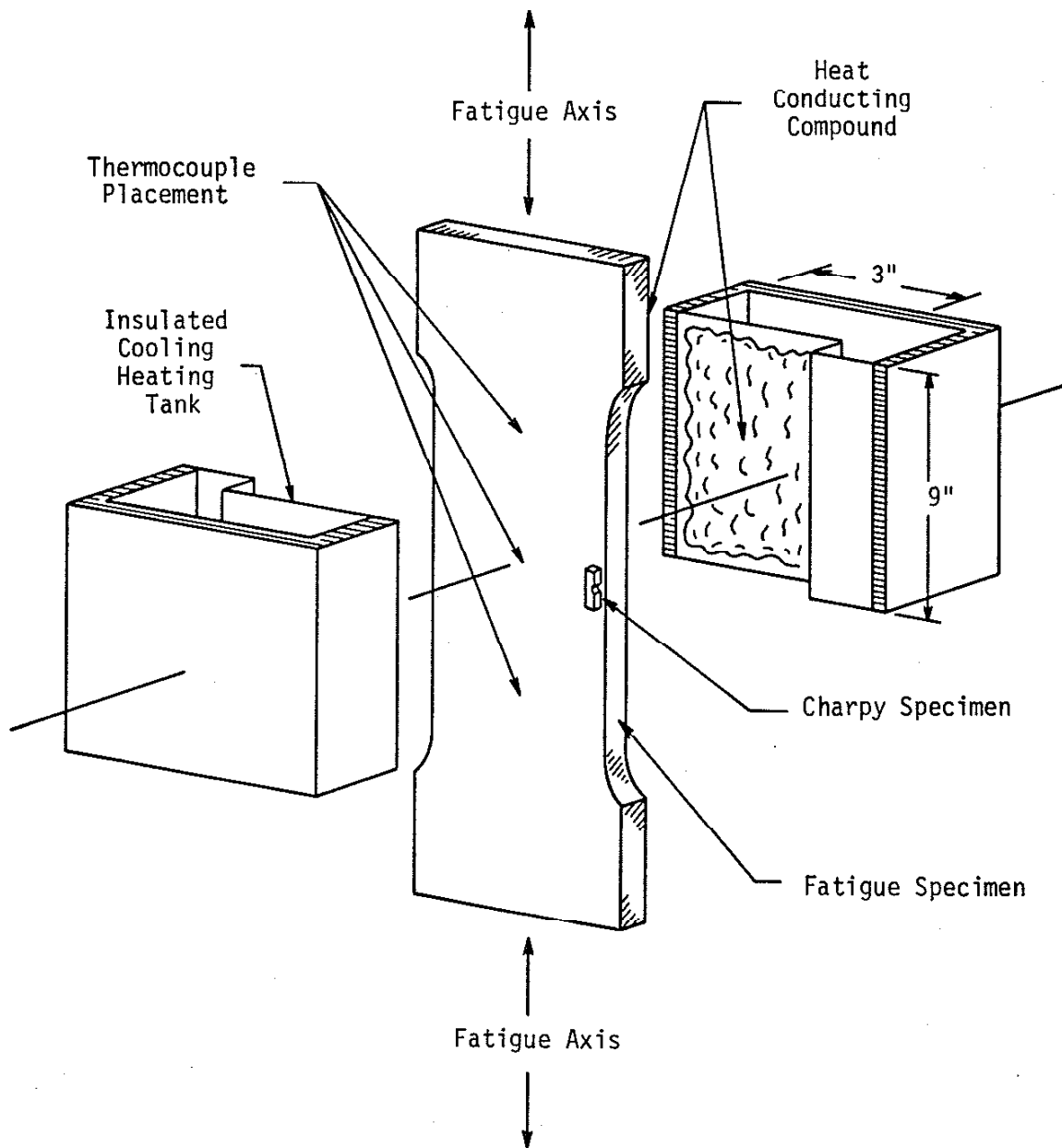3"

9"

Charpy Specimen

Fatigue Specimen

Fatigue Axis

Figure 3.2 Specimen configuration for testing large steel plates
in fatigue in a 300 ton frame. Heating or cooling
tanks are also indicated for controlled elevated or
low temperature testing.

Following fatigue and IPST testing, blocks were cut from the mid-section of each specimen in which standard size Charpy specimens[45] (see Figure 3.3) were machined such that the notch was perpendicular to the normal stress axis. Instrumented impact testing was performed on all of the steels, pre and post-fatigue, to determine the ductile-brittle transition temperature (DBTT), the nil-ductility temperature (NDT), and to find the relative toughness of each. The tests required an impact machine (Tinius-Olsen 359 J (264 ft·lb.) capacity), a load sensor (Effects Technology Model 500 Dynatup System), and a signal display component (HP oscilloscope with memory). The Dynatup System consisted of a pair of strain gauges mounted directly on the striker which sense the compressive force interaction between the impact machine and the test specimen. The load-time profile and integrated energy trace displayed on the oscilloscope was photographed. A report on test procedures, interpretations, and problems published by Ireland[46] was used as a test guideline. The Charpy blocks were tested throughout a temperature range of -120°C to 100°C. Locating tongs were used to accurately position the specimen for each test. For room and elevated temperature tests, a water heating system was used which maintained temperatures to within ± 1°C. The temperature range from room temperature to -60°C was achieved by employing a methonal bath also accurate to within ± 1°C. Below -60°C, specimens were cooled in a liquid nitrogen bath and then taken and placed on the test stand. The temperature, monitored by spot welded thermocouples, was allowed to increase to that desired, and then the specimen was broken by impact. The impact energy
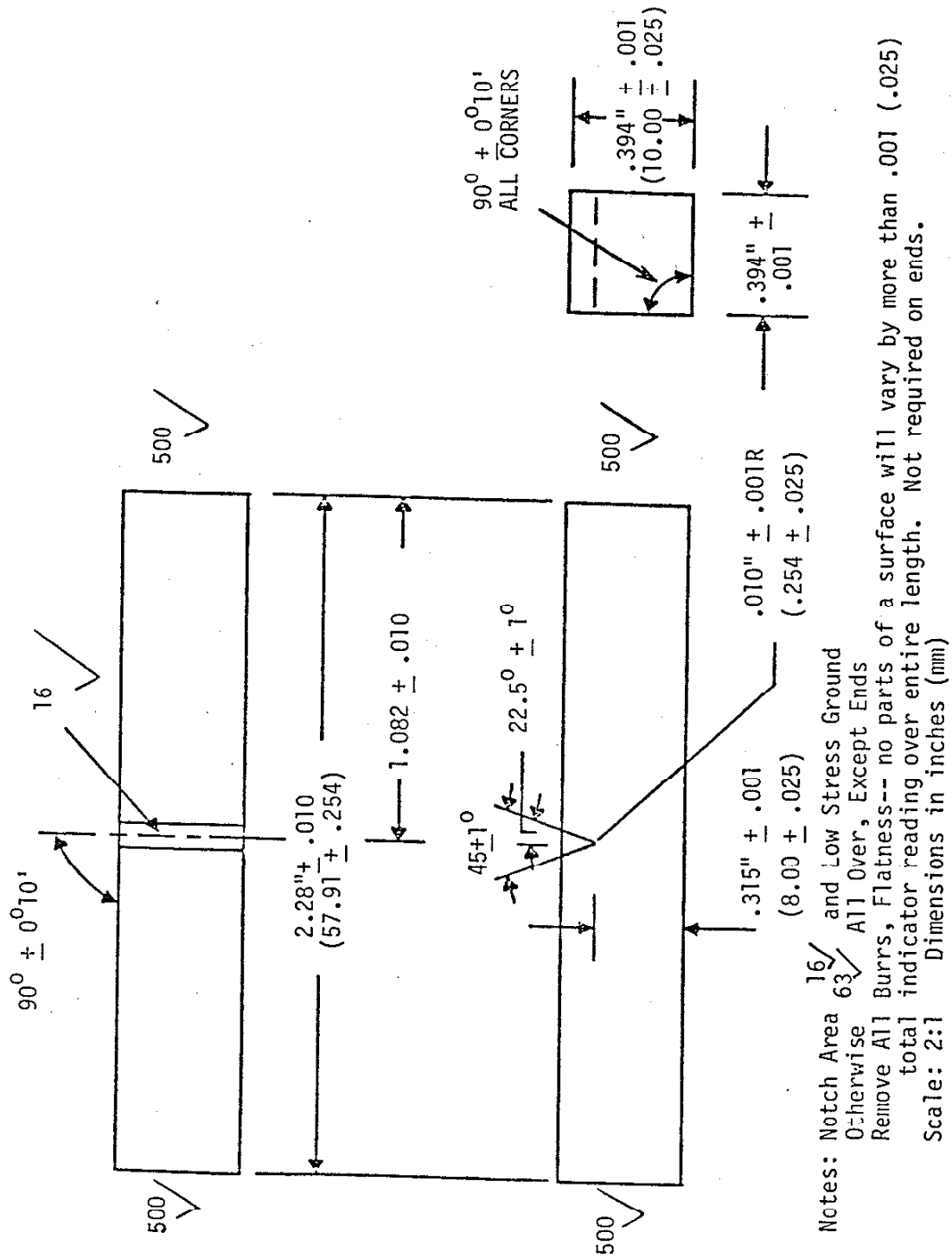
34

Figure 3.3 Charpy V-Notch Impact Specimen.

Notes: Notch Area $\frac{16}{63}$ and Low Stress Ground
Otherwise $\frac{63}{\vee}$ All Over, Except Ends
Remove All Burrs, Flatness-- no parts of a surface will vary by more than .001 (.025)
total indicator reading over entire length. Not required on ends.
Scale: 2:1 Dimensions in inches (mm)

was also recorded by the test stand. Specimen lateral expansion was measured using a micrometer and the fracture surface was inspected to record the percent shear. See Tables 3.2 and 3.3 for experimental procedures and the test matrix. Figure 3.4 presents the experimental procedure in flow diagram format.

Table 3.2 Specifics of Experimental Procedure

Fatigue Tests

- Fully reversed fatigue tests

- Cycling below crack initiation in the elastic regime

- Load controlled tests (Elastic strain)

  Stress amplitude = $\pm$ 30 ksi ($\simeq$ 0.1% strain)

  Mean stress = 0.0 ksi

  Frequency = 3.5 Hz

- 10^4 cycles

- Room temperature & -100 °C for A533B steels

- Room temperature & 100 °C for SAE 1018

Incremental Plastic Strain Test

- Room temperature on A533B Class II

- Maximum strain = 1.0%

Instrumented Impact Tests

- Standard size Charpy blocks

- Temperature range from -120 °C to 100 °C

Table 3.3 Text Matrix and Average Charpy Impact Energy

Steel	Test Temperature			Fatigue Life (cycles)		Charpy Energy @ RT		Nickel Content
	LT	RT	ET	10^4	IPST	AR	10^4	wt%
SAE 1018		X	X	X		20	55	< .05
A533B I AR	X	X		X		170	190	0.53
A533B I HT	X	X		X		110	125	< .05
A533B II	X	X		X	X	170	170	0.60

Fatigue

Stress Amplitude = 30 KSI 207 MPa   AR = As-received (virgin material)
Mean Stress   = 0 KSI 0 MPa   LT = Low Temperature
Frequency   = 3 Hz   RT = Room Temperature
Load Controlled   HT = Heat Treatment (Post Weld)
(Elastic Regime)   ET = Elevated Temperature
                                     IPST = Incremental Plastic Strain Test
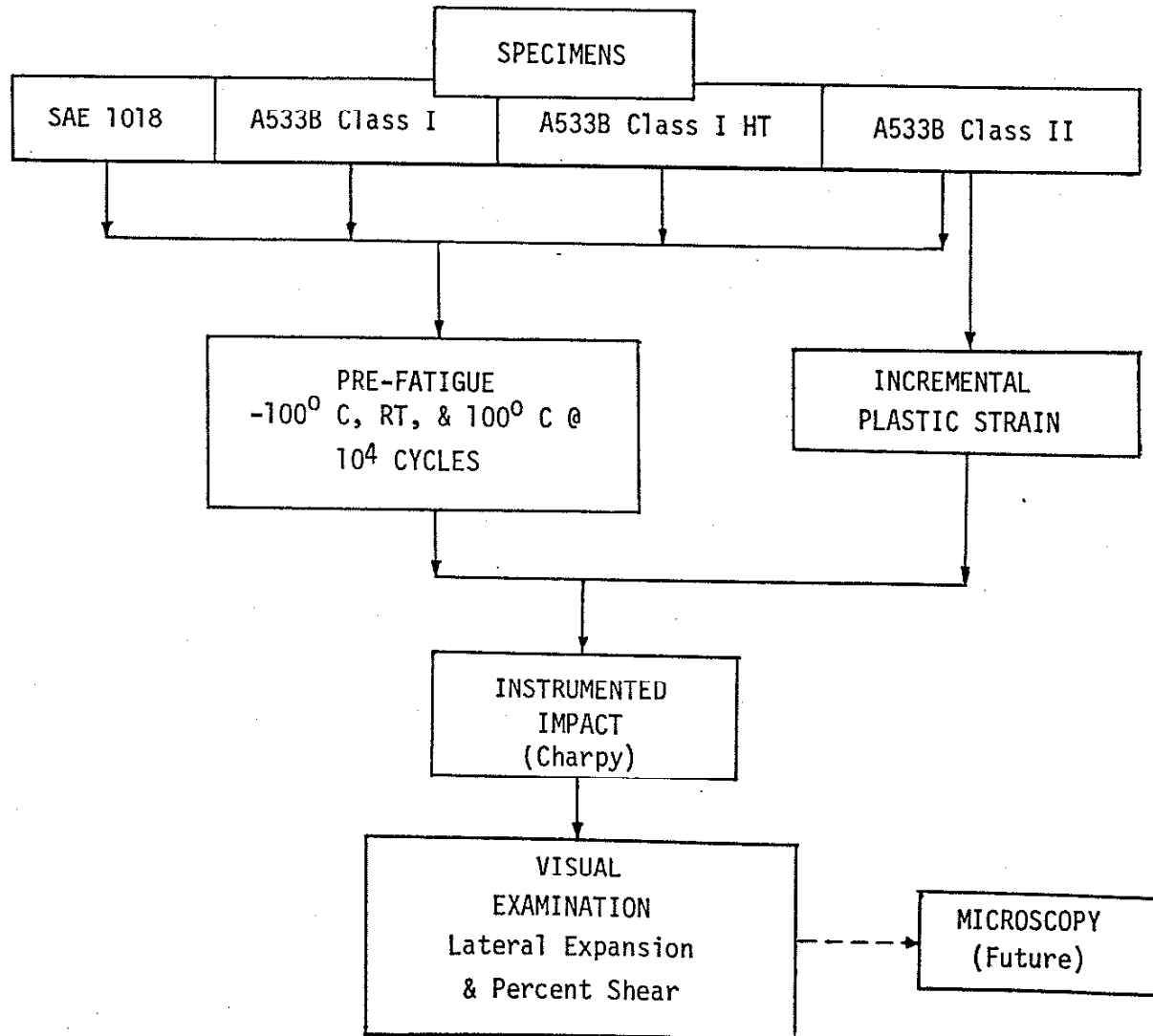
Figure 3.4 Flow Diagram of Experimental Procedure.

4.0 EXPERIMENTAL RESULTS

The SAE 1018 virgin steel possesses a DBTT above normal room temperature and therefore the fatigue test temperatures were chosen at room temperature and +100°C. Using the same reasoning the A533B steels were tested at temperatures of -100°C and room temperature. A stress-strain plot (or hysteresis) from 0 to 10^4 cycles typical of all the steels is presented in Figure 4.1.

Charpy instrumented impact testing revealed the effects of fatigue, if any, on the impact energy absorption behavior throughout the temperature range of -37°C to 100°C and -120°C to RT for SAE 1018 steel and A533B steels respectively. The nil-ductility temperature (NDT) was defined as the temperature corresponding to an absorbed energy at or below 27 J (20 ft·lb.). The DBTT was determined from the Charpy impact energy (CVN) plots, defined as the temperature corresponding to the average between upper shelf energy and lower shelf energy. These temperatures are listed in Table 4.1 for each steel.

Marked differences were seen in the impact behavior of A533B Class I HT steel. The apparent effect resulting from fatigue was increased ductility revealed by a shift of the NDT and DBTT. The changes can easily be seen in Figure 4.2 where the NDT shifted 25°C, down to -40°C and the DBTT shifted 10°C, down to -15°C. The two fatigue conditions, 10^4 @ LT and 10^4 @ RT, exhibited virtually identical differences when compared with results of virgin material. No significant changes in upper shelf energy of 190 J (140 ft·lb.) were discernible from the available data.
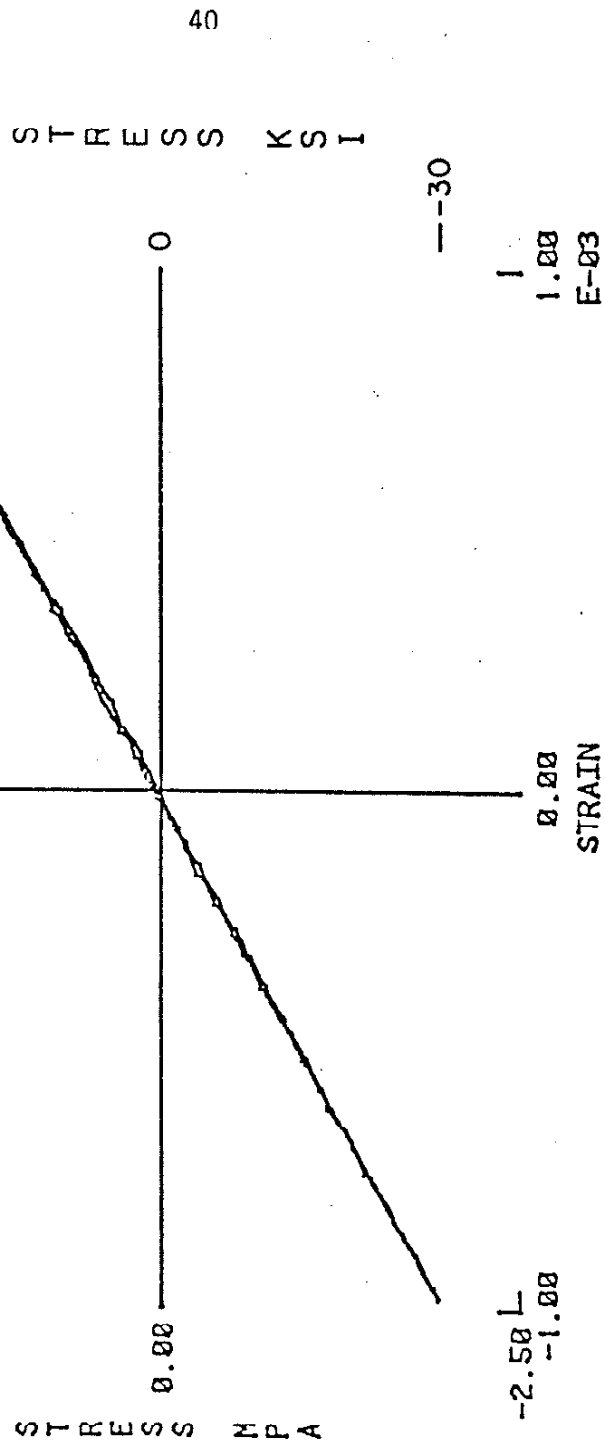
Figure 4.1 Typical stress-strain plot for SAE 1018 and A533B steels for 1.0 to 10⁴ cycles.[47]

Table 4.1 The maximum load, average maximum load, ductile-brittle transition temperature, and nil ductility temperature of SAE 1018 and A533B steels from Charpy impact data.

Steel	Pre-Fatigue Condition	P_{max}(kN)	P_{ave}(kN)	DBTT(°C)	NDT(°C)
SAE 1018	AR	13.34	13.34	35	23
	10^4 @ ET	14.68	14.68	25	5
	10^4 @ RT	14.68	14.68	25	15
A533B I HT	AR	NA*	17.35	− 5	−15
	10^4 @ RT	19.13	17.79	−15	−40
	10^4 @ LT	19.13	17.79	−15	−40
A533B I	AR	20.02	18.68	−50	−65
	10^4 @ RT	22.24	20.02	−75	−95
	10^4 @ LT	22.24	20.02	−75	−95
A533B II	AR	NA*	22.24	−90	−120
	10^4 @ RT	22.69	20.46	−90	−120
	10^4 @ LT	22.24	20.91	−90	−120
	IPST	24.02	10.91	−90	−120

NA*, not enough photographs available
AR = as received

A similar, more significant shift in NDT and DBTT occurred for A533B Class I steel. In this case, as before, both fatigue conditions produced identical results. The NDT shifted from -65°C to -95°C, the DBTT decreased from -50°C to -75°C. The results are presented in Figure 4.3.

The SAE 1018 steel displayed a behavior similar to the A533B Class I HT steel. Here the NDT showed a more pronounced alteration than did the DBTT, that from 23°C to approximately 0°C. The DBTT shifted from 35°C to 25°C and once again these shifts appeared to be independent of fatigue test temperature. Note that for the above materials, the temperature changes are approximate to about ± 3°C. The upper shelf energy for SAE 1018 appears to be about 136 J (200 ft·lb.) as shown in Figure 4.4.

The A533B Class II steel showed no distinguishable effects from fatigue, either at RT or LT, when compared to the as-received material. The pre and post fatigue conditions displayed an NDT of less than -120°C, a DBTT of -90°C, and an upper shelf energy of approximately 230 J (170 ft·lb.). One specimen of this steel was subjected to an incremental plastic strain test. Charpy blocks cut from the IPST material exhibited identical behavior (no change) to the other conditions of this steel. (See Figure 4.5).

The lateral expansion and percent shear were measured for each specimen. These measurements facilitated the curve fitting process by indicating the relative ductility of each specimen. The greater the
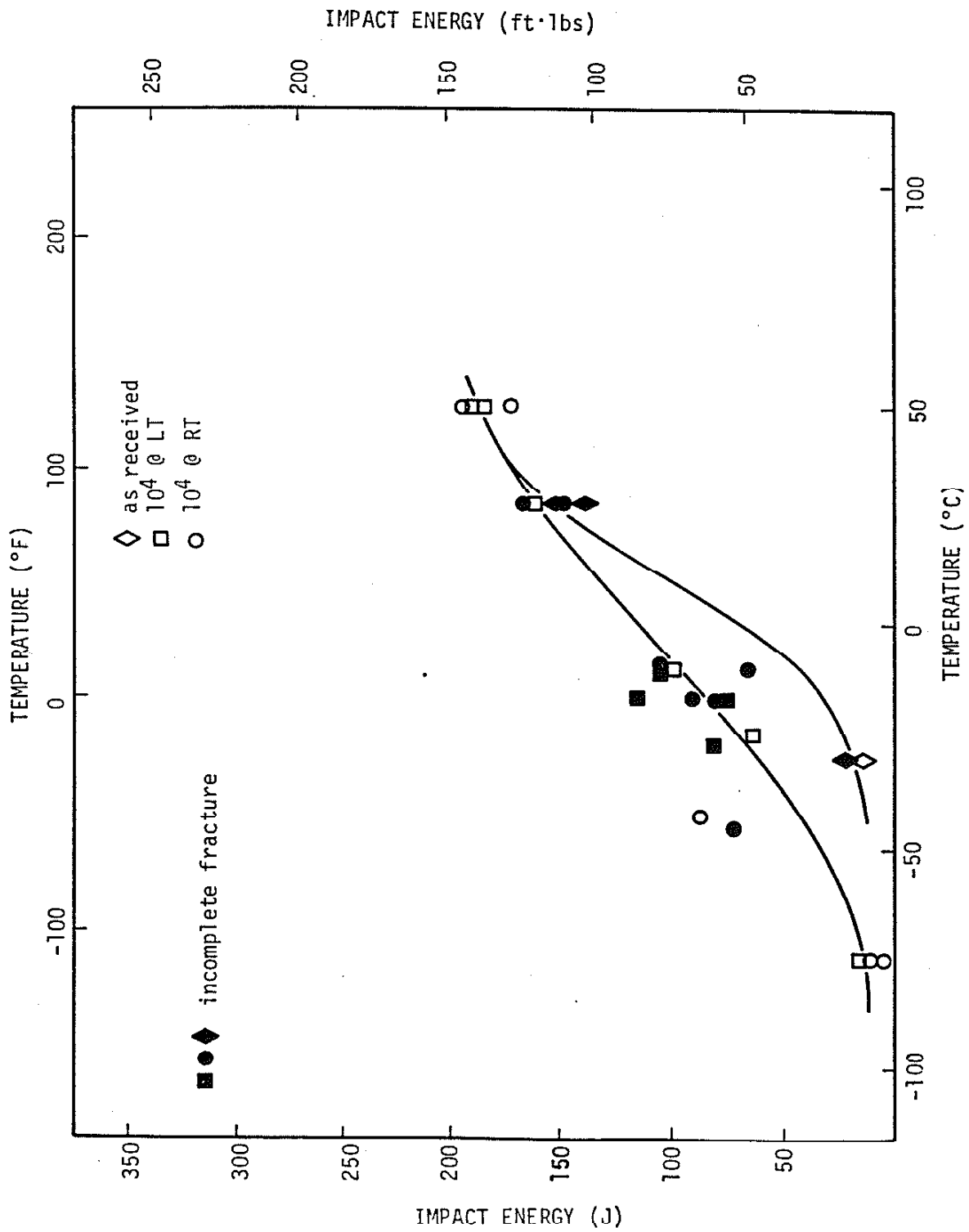
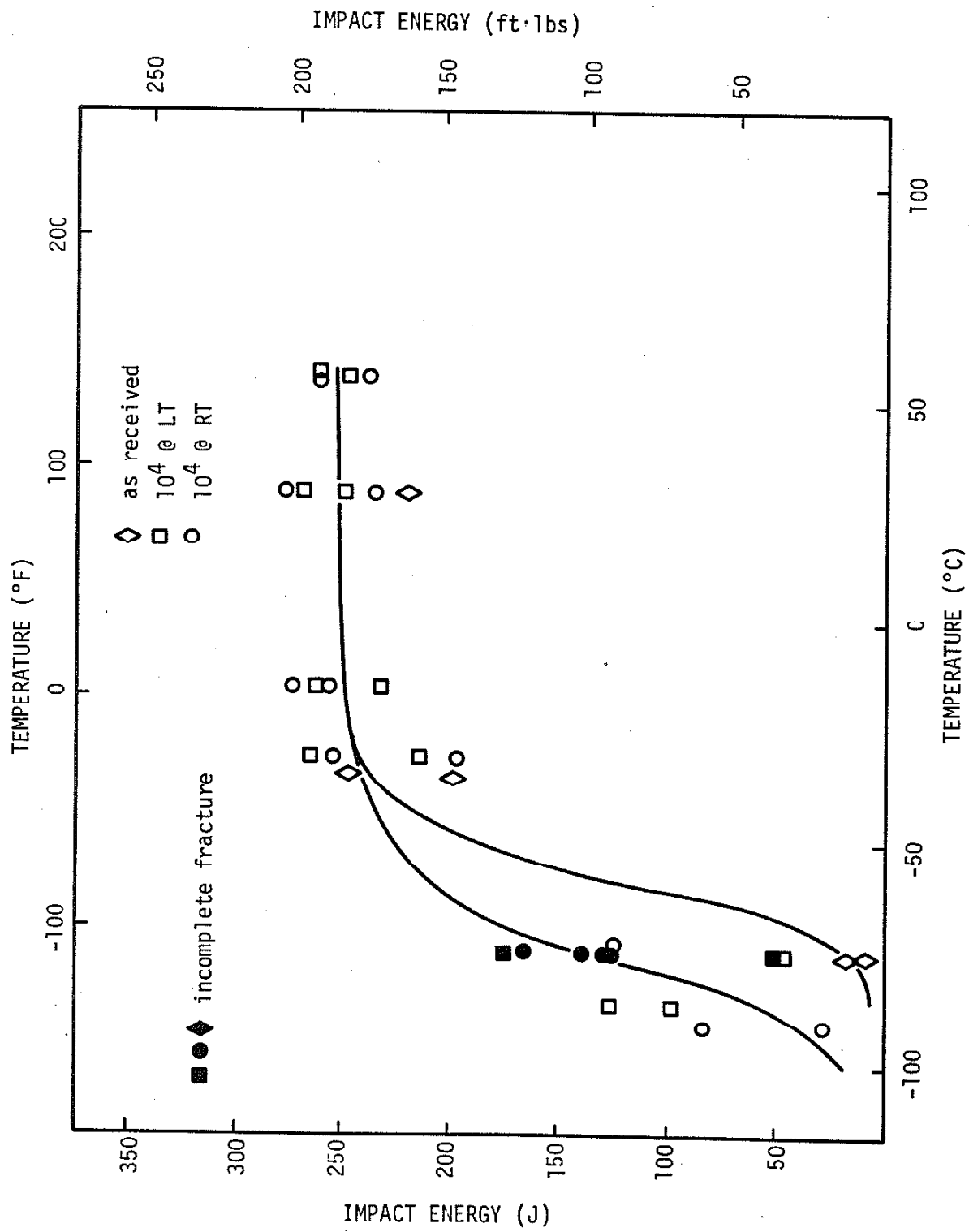Figure 4.2 Impact Energy versus temperature for A533B Class I HT steel.

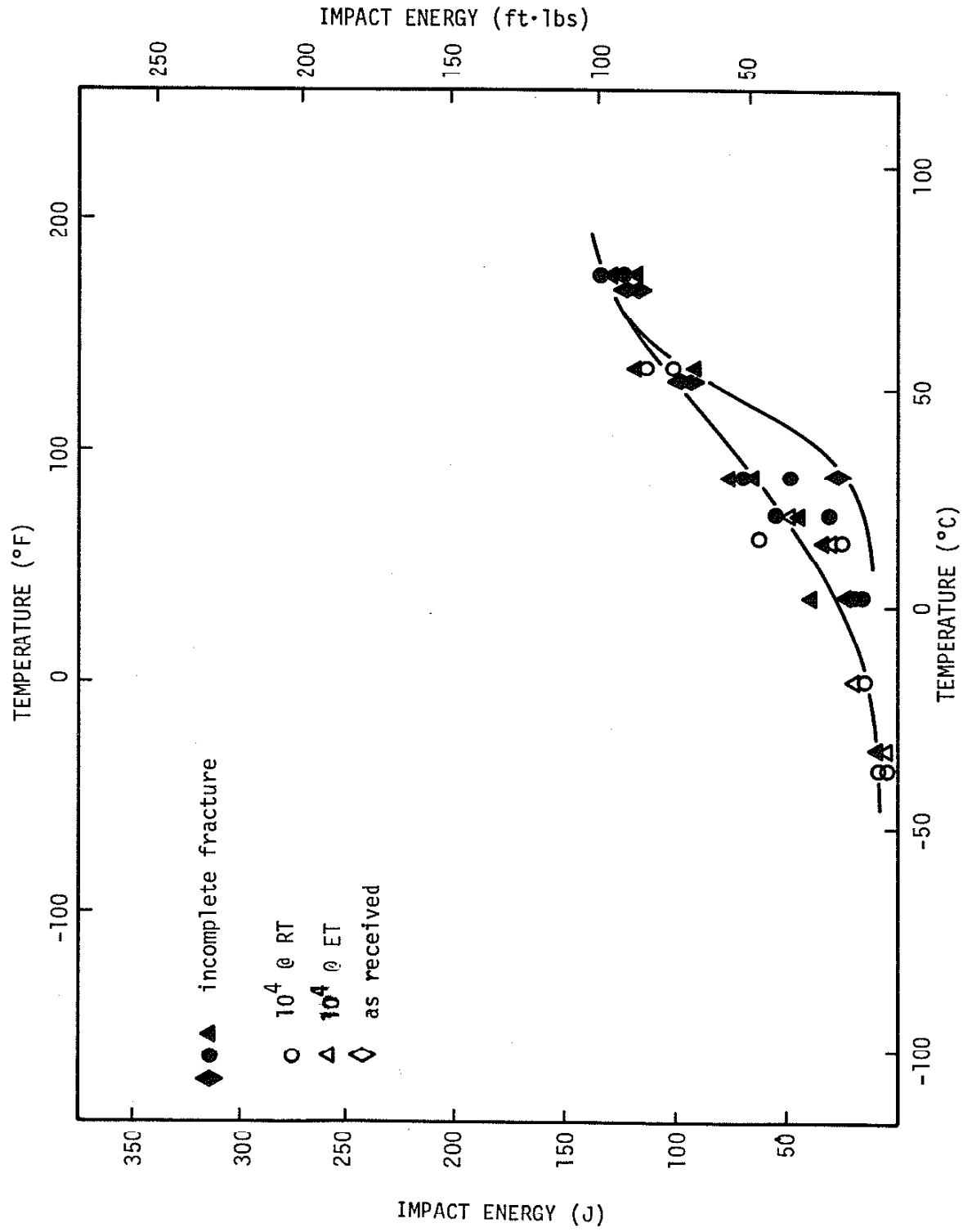Figure 4.3 Impact Energy versus temperature for A533B Class I steel.

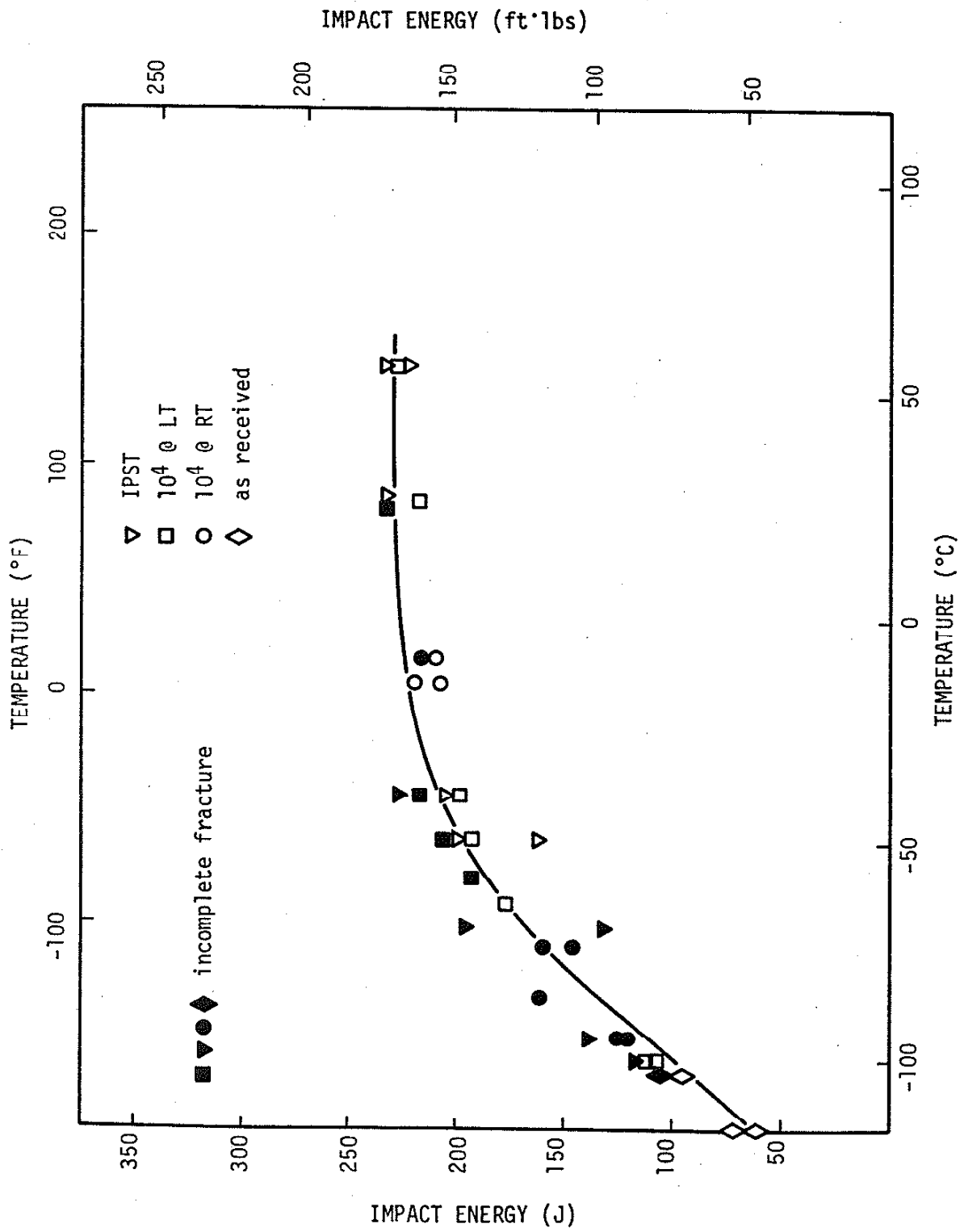Figure 4.4 Impact energy versus temperature for SAE 1018 steel.

Figure 4.5 Impact energy versus temperature for A533B Class II steel.

lateral expansion or percent shear the more ductile the material. These results are presented in Figures 4.6 through 4.9 and follow the general trend of the CVN results.

The load-time traces and integrated energy curves were recorded by photographing oscilloscope displays. A typical result is shown in Figure 4.10. The load-time trace can be used to determine the approximate crack initiation time and crack propagation time. Integrating the area under this curve up to these points yields the crack initiation and propagation energies. The integrated energy record serves as a good comparison with the dial energy recording.
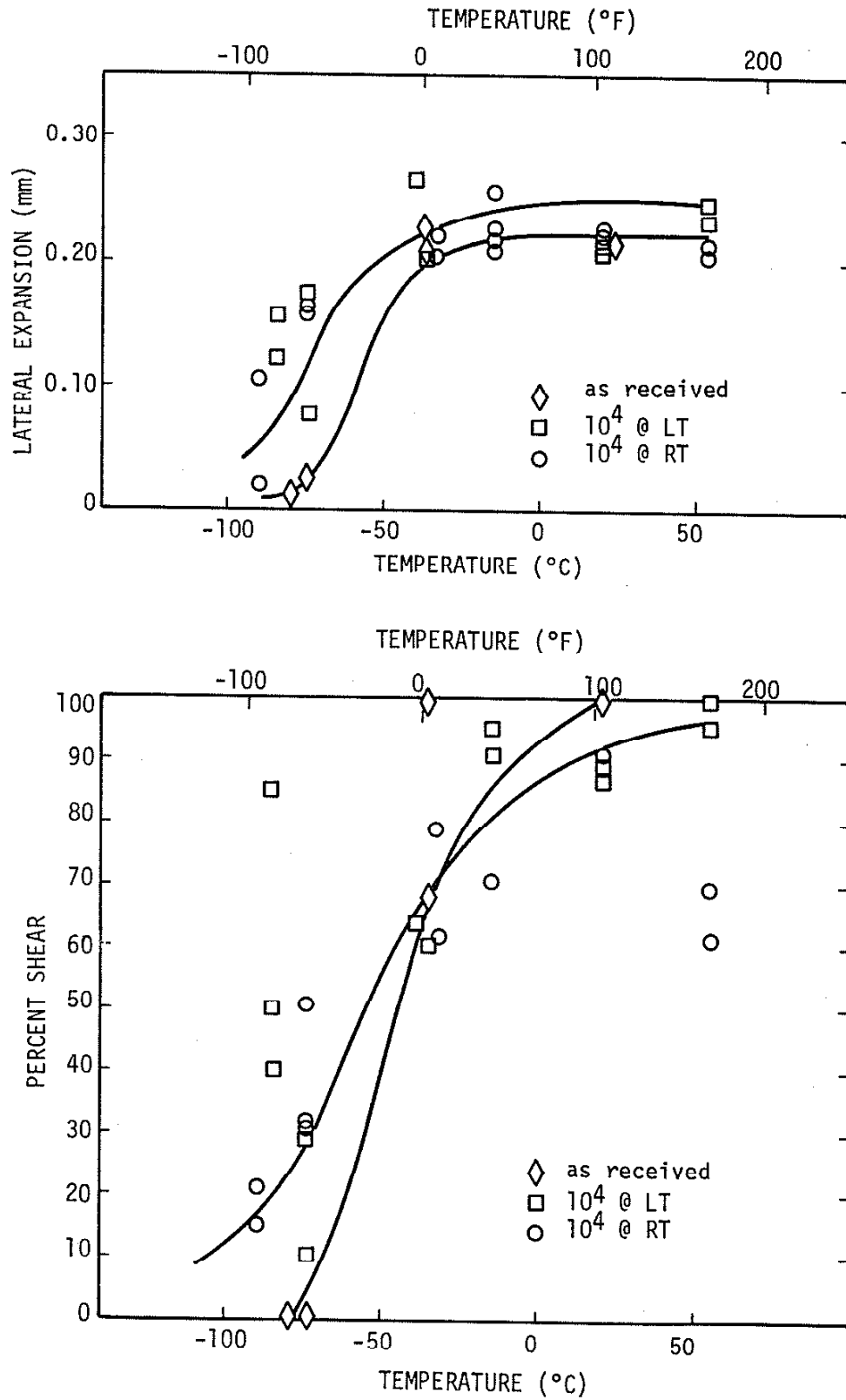
Figure 4.6   Lateral expansion and percent shear versus
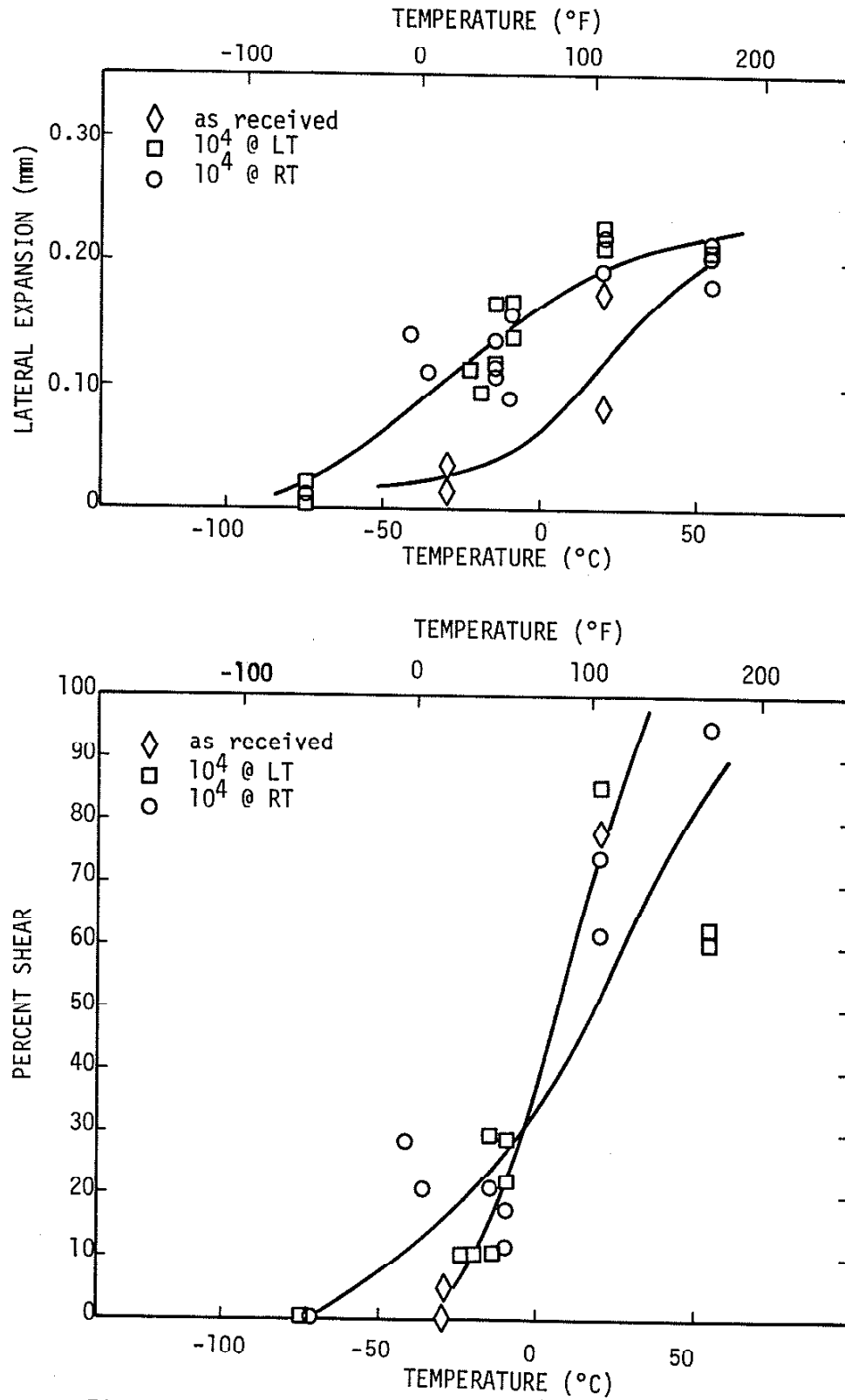temperature for A533B Class I steel.

Figure 4.7 Lateral expansion and percent shear versus temperature for A533B Class I HT steel.
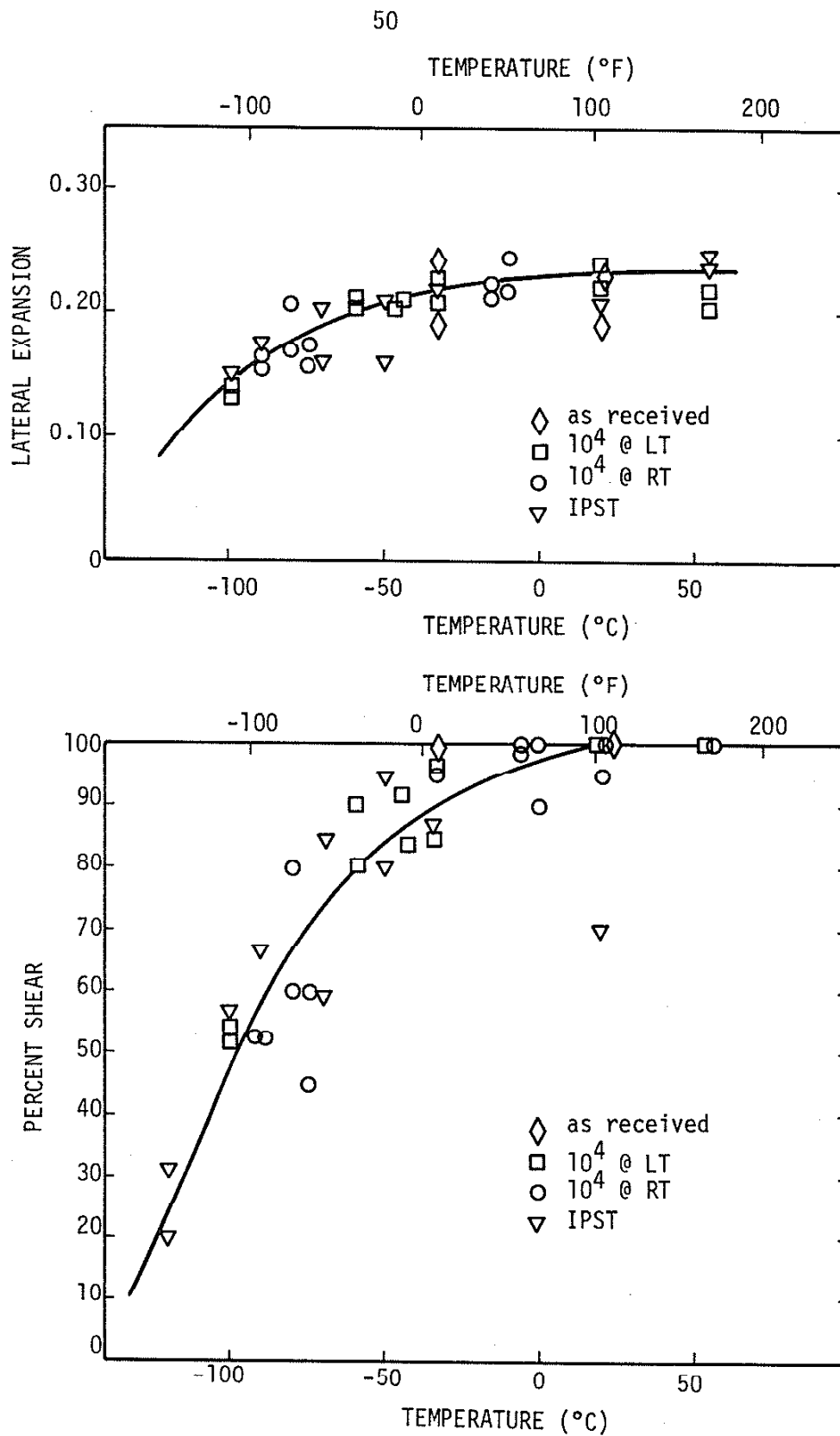
Figure 4.8 Lateral expansion and percent shear versus temperature for A533B Class II steel.
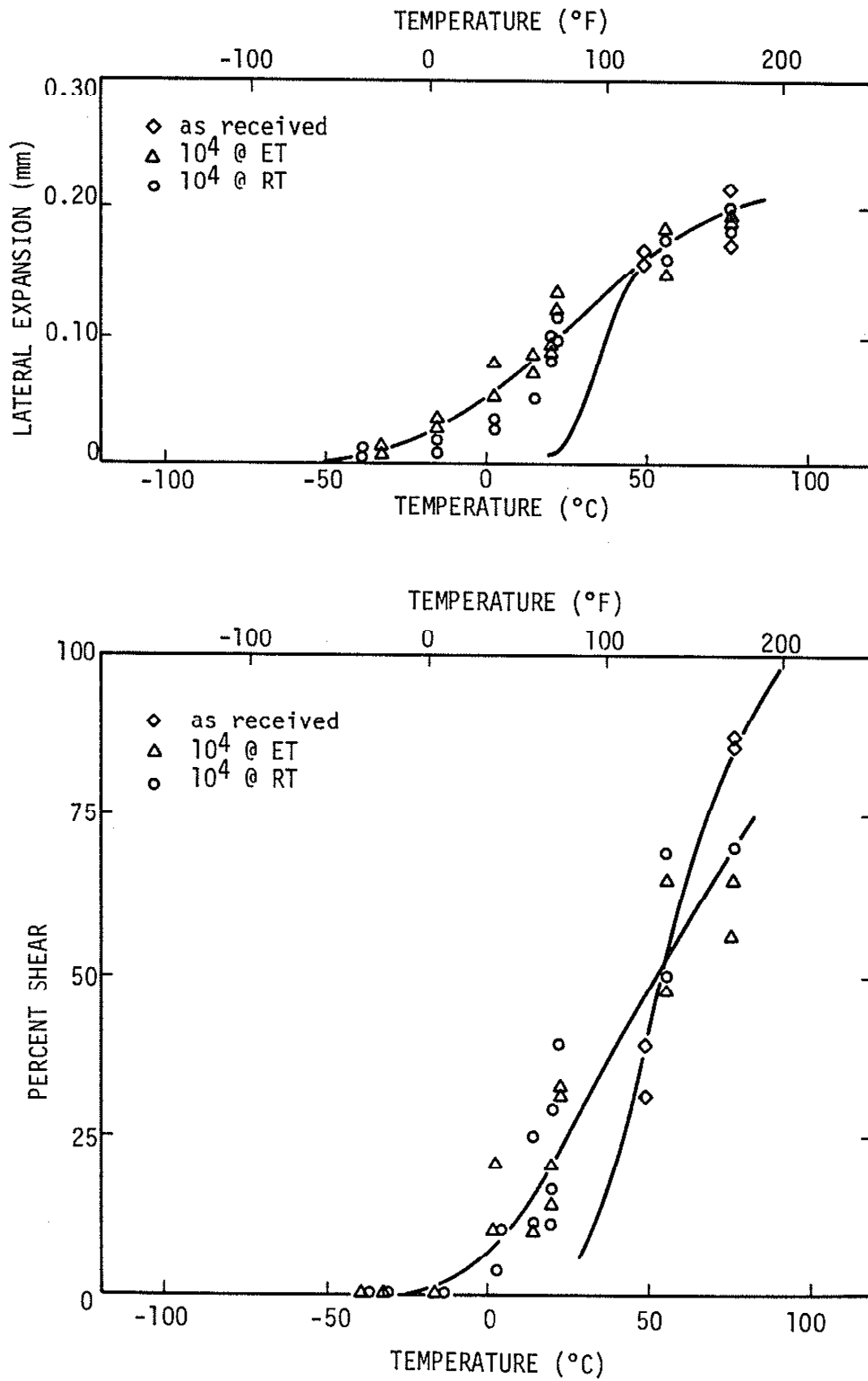
Figure 4.9 Lateral expansion and percent shear versus temperature for SAE 1018 steel.
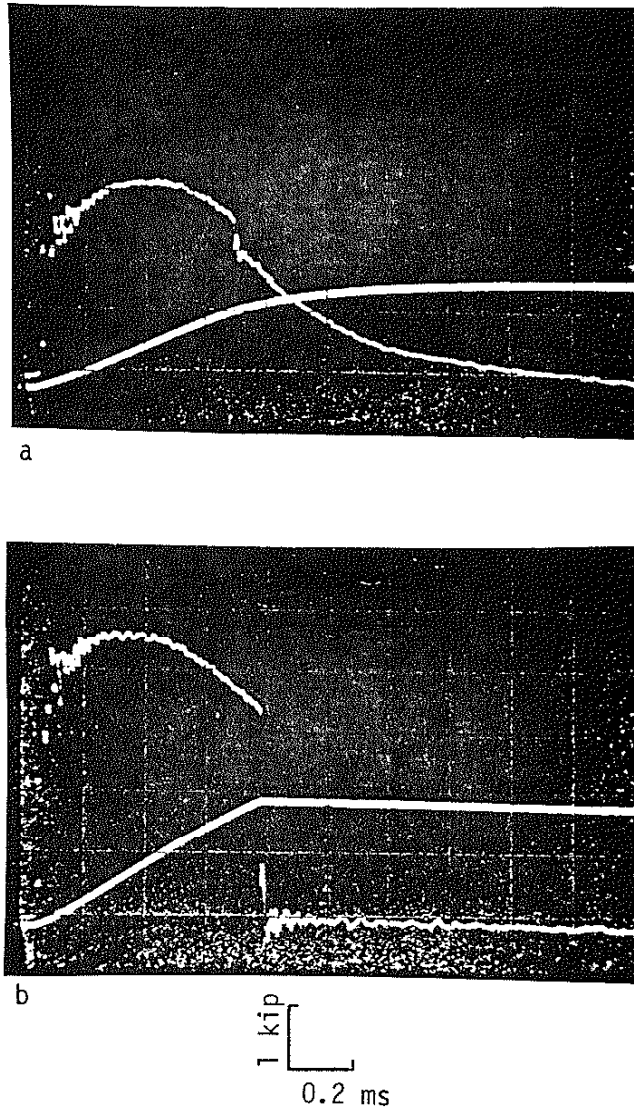
Figure 4.10   Load vs. time oscilloscope traces
              for (a) SAE 1018 on the upper shelf
              and (b) A533B Class I at the DBTT.

5.0 DISCUSSION

5.1 History of Materials and Problems During Testing

The SAE 1018 and A533B steels were provided from the same stock of material as used in Riedy's investigations.[47] Riedy performed elastic fatigue tests similar to those performed in this project. His results include scanning electron micrographs (SEM) and transmission electron micrographs (TEM) which provide a reasonable prediction of the micro-structural alterations expected from the elastic fatigue.

The two specified test temperatures for each steel were chosen in order to make a comparison between brittle and ductile elastic fatigue effects. The CVN data, which will be discussed subsequently, suggests that the elastic fatigue effects on impact properties are independent of test temperature.

Although the surface temperature was monitored by thermocouples, for LT and ET tests, no method was available to regulate gradients in the temperature distribution. The ET fatigue test possessed a very flat temperature distribution whereas the LT fatigue tests witnessed distinct temperature perturbations. It is most likely that the thermocouple readings were erroneous and that the actual surface gtadients were less. The uniformity of the temperature distribution fortunately was not as important as maintaining the temperature below the DBTT. Here the steel was assumed to have behaved in a uniformly brittle fashion because the physical properties remain constant within the uncertainty.

5.2 Instrumented Impact Testing Definitions

The instrumented Charpy impact test provides such useful information as the load versus time and energy versus time (integrated) traces. These are used to specifically determine the maximum load to fracture, the crack initiation energy, and the crack propagation energy. The maximum load to fracture clearly is the highest point which appears on the load versus time trace. However, there is some disagreement on the definitions of the crack initiation energy and the crack propagation energy. Hertzberg[1] has defined these energies as shown in Figure 5.1, where the initiation energy is the area integrated under the load versus time curve past the maximum load and up to the first large drop in load. The propagation energy is the integrated area under the remainder of this curve. This does not seem intuitively correct when considering the change in behavior from brittle fracture to ductile fracture. In brittle fracture the curve typically reaches the maximum load and then sharply decreases immediatley afterwards. The propagation energy must therefore be very little, which appears to be correct. Now when the fracture becomes more ductile the curve broadens but the magnitude and time to maximum load are reasonably constant. Because of this behavior, it is believed that the initiation energy is also fairly constant, as this trend was observed in each steel under investigation. Therefore as the temperature increases and the metal becomes ductile, the propagation energy is the area under the load versus time curve integrated from the maximum load to the curve end as in Figure 5.2.
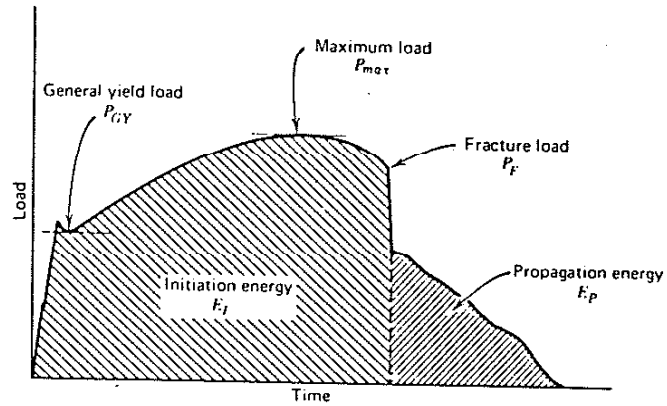
Figure 5.1   Iniation energy and propagation energy
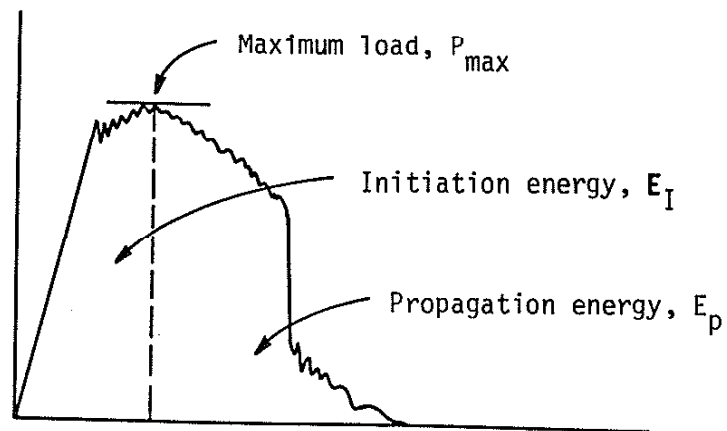as defined by Hertzberg[1].

Figure 5.2   Initiation energy and propagation energy
as defined by Canty.

5.3 Fatigue Effects Upon CVN

The load versus time Charpy impact trace photographs were analyzed using the aforementioned definitions. The traces were photographed throughout the temperature ranges of interest and several similarities were observed between the upper temperature fatigued and lower temperature fatigued groups of each respective steel.

Three of the four steels incurred a net shift of DBTT and NDT towards lower temperature values. The exception was the A533B Class II steel which showed no marked effects from the fatigue. All the steels showed an increase in the dislocation density and the creation of some dislocation subcells directly from the 10^4 cycles.[47] The buildup in the dislocation population is a complex and chaotic process which may in part be used to explain why toughness and ductility increase. The shear stress required for further deformation is comprised of two quantities, the effective shear stress and the internal stress. The effective shear stress arises from the interaction of the dislocations with short range obstacles i.e. isolated dislocations, whereas the internal stress arises from long range obstacles. Complex dislocation arrays, which may be developed from fatigue, provide long range obstacles which strongly affect the internal stress. The flow stress increases which in turn provides further resistance to crack advancement. The increase in the dislocation density may contribute to a subsequent increase in plasticity around the crack tip and would allow the steels to flow in a plastic manner at lower temperatures. This then increases the energy absorption and accounts for increased ductility.

The lateral expansion and percent shear measurements were used along with Charpy energy readings and the load versus time traces to determine the best fit curves on the impact energy versus temperature plots. See Figures 4.6 through 4.9

In some instances where the curve appears to deviate from data points, an adjustment was made depending upon how brittle or ductile the other measurements proved to be. For instance, if the impact energy was low but the percent shear and lateral expansion were high, the material was still ductile. This allowed the curve to remain on the high side around this temperature even if nearby points deviated considerably. This was a way of getting a better "feel" for what the data represented.

It is important to point out a potential concern with the low temperature Charpy tests. The specimens were put into a liquid nitrogen bath and allowed to cool. The temperature was monitored by chromel-alumel thermocouples that had been spot welded onto the surface of each specimen. Each specimen was pulled from the bath and placed on the test machine anvil where it was carefully watched during warm up. When the desired surface temperature was met the impact event took place. It is possible that a temperature gradient existed in some part of the specimen. Nevertheless, this is standard CVN testing procedure.

It is likely that the surface temperature was greater than the center temperature so that the specimens would have behaved in a more brittle fashion. Data points may belong at lower temperatures therefore the predicted DBTT may be conservative.

5.4 Load Versus Time Trace Analysis

The A533B Class I steel, fatigued at RT, had a constant average load of about 4.0 MN (4.5 kips) with the maximum load occurring at the DBTT. Only the traces recorded at -75°C showed the maximum load, P_{max}, of 4.45 MN (5 kips). It was not possible to distinguish separate Charpy curves for the RT and LT conditions because of virtually identical results. The characteristic load jump right at the DBTT was observed in all the fatigued A533B steels. At the DBTT the brittle and ductile fracture mechanisms compete with each other on a microscopic scale and the micromechanisms of this behavior are not known.

It is of interest to distinguish the fracture behavior at different temperature ranges. At low temperatures, i.e. T < NDT, cleavage controlled fracture was observed with abrupt crack extension and no stable crack growth. As the DBTT is approached, the fracture is still cleavage controlled but small amounts of deformation occurs around the crack tip (blunting). At higher temperatures approaching the upper shelf fracture toughness, ductile tearing preceded cleavage rupture and load-time traces exhibited gradual drops in the load with distinguishable, abrupt load drops at large times. Similar behavior with no abrupt load drops are noted at still higher temperatures well into the upper shelf regime.

The load versus time traces for all other A533B steels followed the same trend. Figure 5.3 shows the change in load history over the transition range for A533B Class I AR steel. At low temperatures (Fig. 5.3a), the sharp drop after maximum load, P_{max} was indicative of brittle
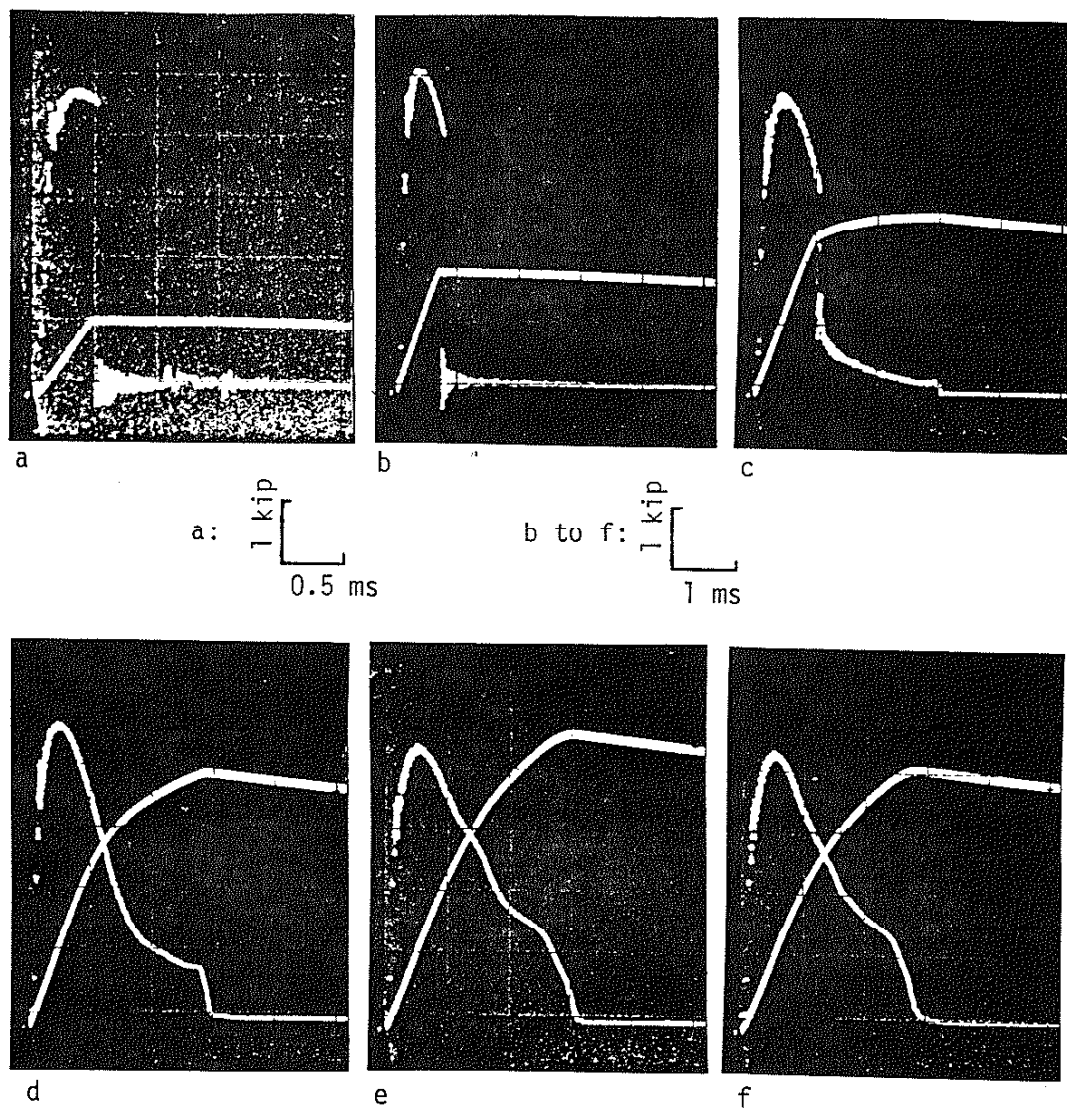
Figure 5.3 Load vs. time traces for A533B Class I steel at
(a) -90°C, (b) -75°C, (c) -33°C, (d) -15°C, (e) RT,
and (f) 55°C. Note: change in scale from a to b
through f.

fracture with virtually no plastic flow. At the DBTT (Fig. 5.3b), the trace became broader and the energy absorption increased. The propagation energy requirement increased due to the small amount of plastic flow. An increase in P_{max} can be seen which suggests an increase in initiation energy also exists. As the temperature increased the traces became much broader but P_{max} returned to its original value (Fig. 5.3 c, d, e, and f). The initiation energy remained constant as the temperature increased which directly implied that the fracture was propagation controlled. At the end of the impact event there existed a sharp drop in load where the remaining cross section in front of the crack tip had yielded catastrophically or in the case of incomplete fracture the specimen had deformed enough to fly off the test stand. The SAE 1018 steel exhibited like behavior, however, the increase in P_{max} at the DBTT did not occur. The duplicate behavior of the specific fatigue groups of steels argues strongly that the elastic fatigue effects on impact properties is independent of fatigue test temperature. Table 4.1 lists the DBTT, NDT, P_{ave}, and P_{max} for all the steels. P_{ave} is the average maximum load over the temperature range. This idea is also supported by the crack initiation behavior. Since the initiation energy varies so little with temperature change, the fatigue damage received remains constant with temperature also. On the microscopic level, the same size and distribution of microcracks develop no matter what the temperature is. The stresses applied were well within the elastic regime, below which the brittle and ductile crack initiation mechanisms operate. The results indicate temperature independent crack initiation after elastic fatigue in these steels. In this investigation the fatigue effects seem

to be beneficial as the ductility increased and the upper shelf impact energy remained unchanged.

In a comparison between A533B Class I and A553B Class I HT, the former possessed a significantly higher ductility at lower temperature. The addition of nickel to the chemical composition is believed to account in part for the difference in ductility.

As an extra check of the data, the impact energy was determined using the method of Ireland.[46]   The energy consumed by bending the specimen E_{SD}, can be related to the energy from the energy-time record E_a, and the system's energy capacity E_o as

$$E_{SD} = E_a \left(1 - \frac{E_a}{4E_o} \right)$$ (5.1)

The values obtained were conservative but within about 0.1 deviation from the dial readings. Sample calculations are shown in the Appendix.

5.5 Fracture Toughness-CVN Correlations Upper Shelf

The correlations discussed in Sec. 2.0 above were used to predict the effects that elastic fatigue cause on the SAE 1018 and A533B steels. Data was compiled from several sources for comparison with the correlations to determine their overall usefulness. A comparison of the CVN values reveals that these particular heats of the A533B steels possess significantly higher upper shelf energies. The predicted values of K_{Ic} for A533B Class I AR and HT steels using the Roberts and Newton and Barsom and Rolfe correlations are presented in Figure 5.4. The Roberts
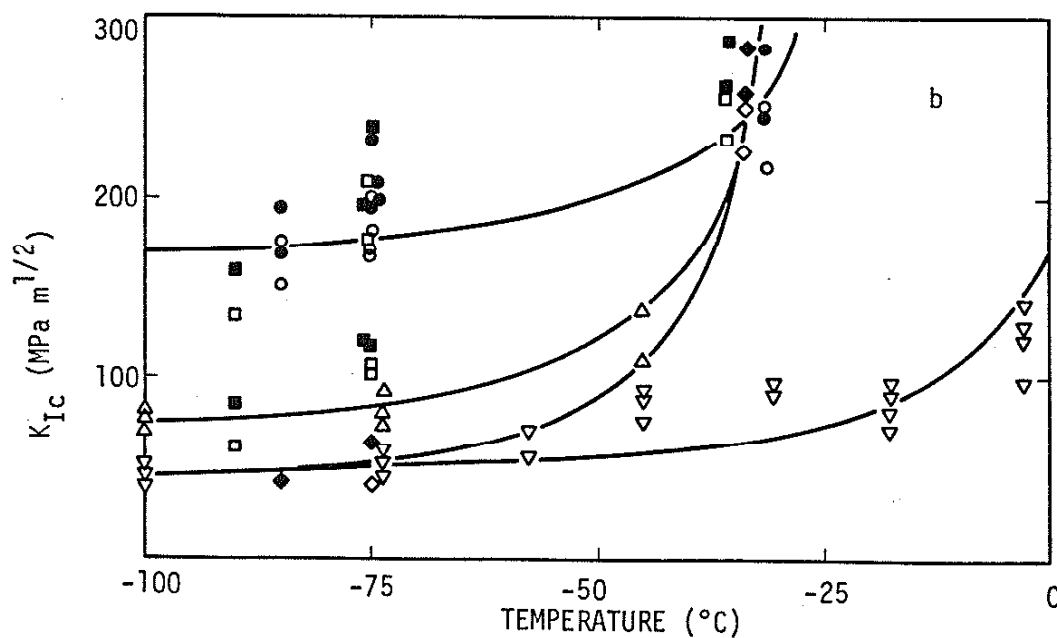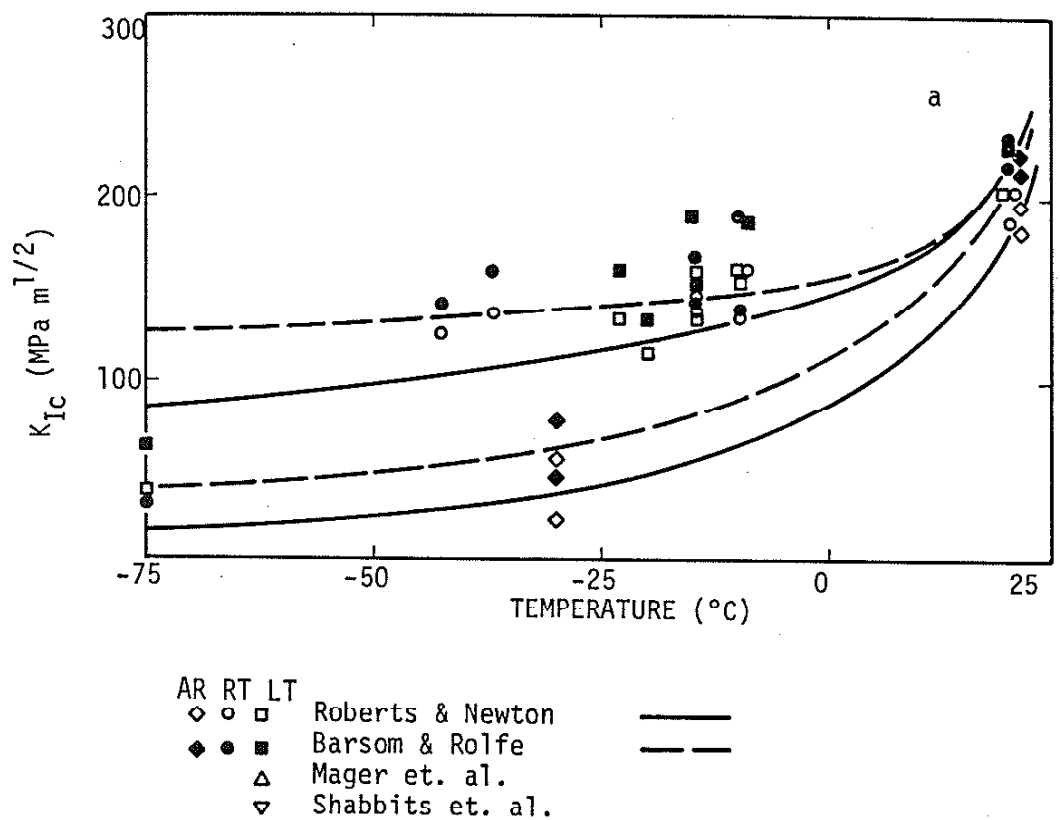
Figure 5.4   Fracture toughness as a function of temperature for
(a) A533B Class I HT steel and (b) Fracture toughness
as a function of temperature for A533B Class I steel

and Newton correlation is slightly more conservative, however both correlations yield values of K_{Ic} greater than expected when compared with K_{Ic} data from Mager et al.[48] and Shabbits et al.[49] The correlations here are being used at the beginning of the upper shelves in an effort to be more effective since a variation of upper shelf energy with temperature may not provide a consistent evaluation of the toughness. Data is plotted for as received steel as well as fatigued steel. An increase in K_{Ic} can be seen for the latter condition. The actual magnitude of toughness predictions is not as meaningful as the accompanying trend. The increase in K_{Ic} causes the curve to shift to the left, to lower temperatures as shown in the figure. This tendency predicts that possible beneficial effects or at least no detrimental effects result from elastic fatigue. The same result is expected for the A533B Class II and SAE 1018 steels due to the nature of the CVN results.

5.6 Fracture Toughness-CVN Correlations Transition Region

The fracture toughness of A533B Class I AR steel as predicted using the Sailors and Corten correlations is plotted in Figure 5.5. There is good agreement between predictions for virgin material and the trend band of data for this steel (See Figure 5.6). The correlation was developed for the range of CVN values between 7 and 68 J (5 and 50 ft·lbs) but due to the relatively large upper shelf values the correlation may be valid up to much higher values. The comparison between the AR and fatigued conditions revealed the same shift trend for K_{Ic} and
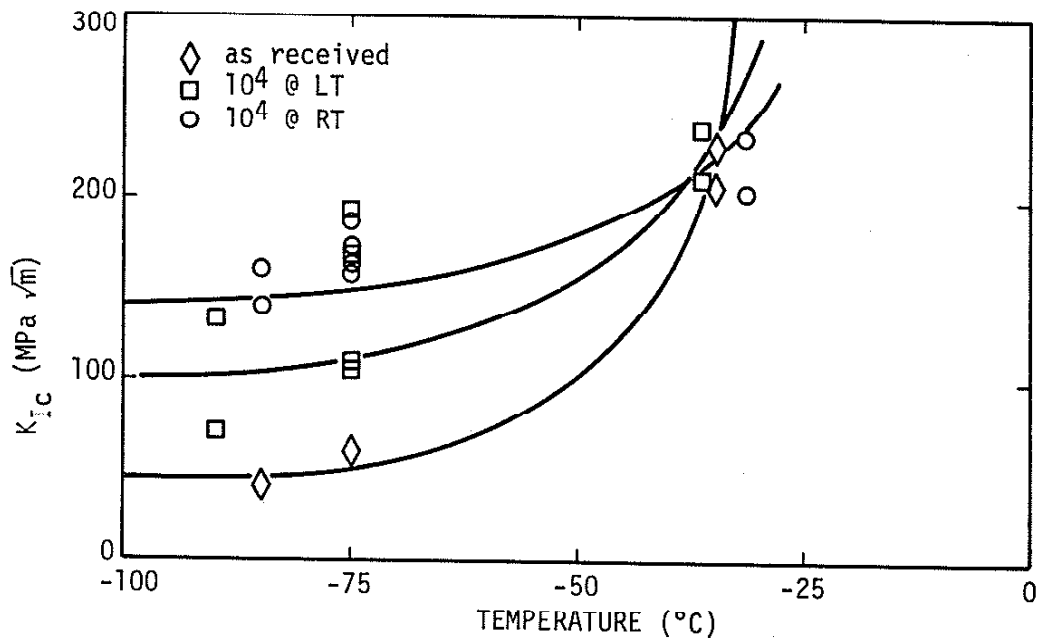
Figure 5.5 Fracture toughness determined using the Sailors and Corten correlation for A533B Class I steel

Figure 5.6 The trend band of data for A533B Class I steel after Odette and Lucas[7].
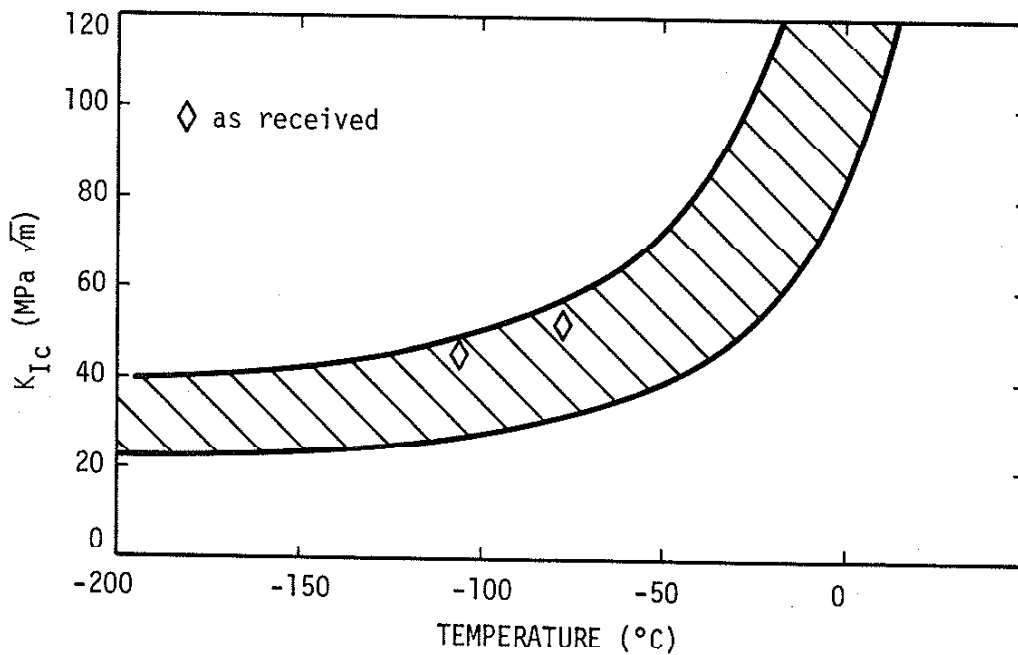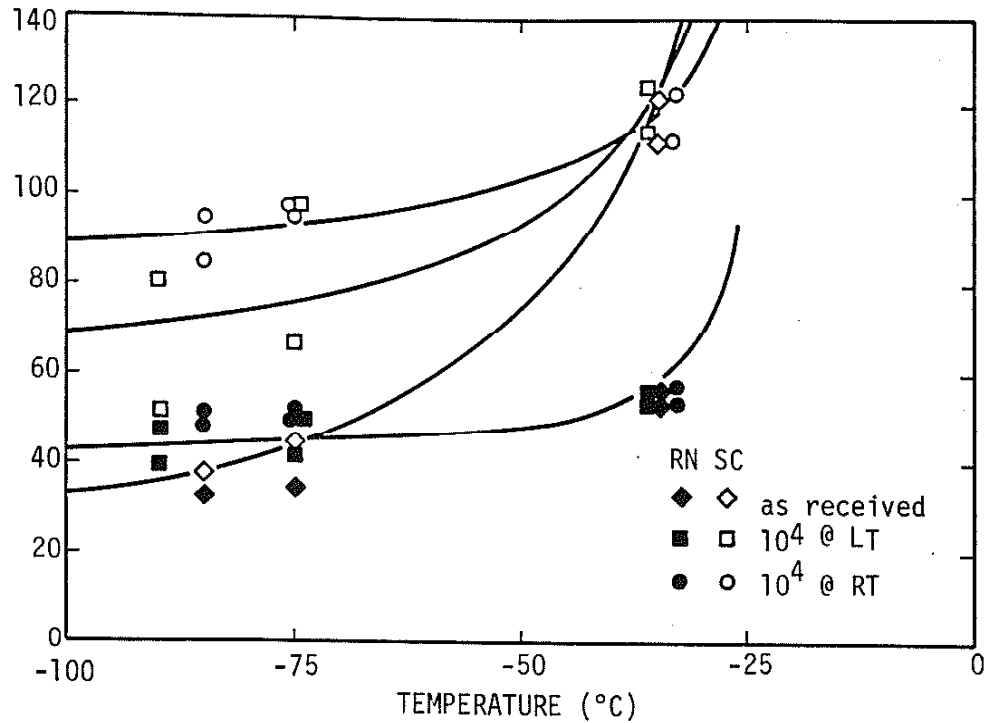
Figure 5.7 Dynamic fracture toughness determined using the
Roberts and Newton (RN) and the Sailors and
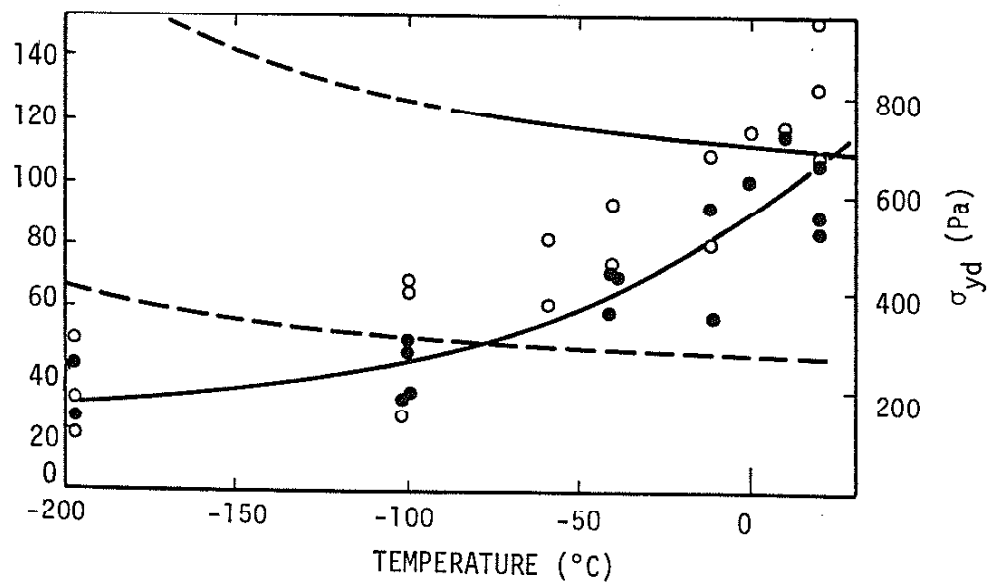Corten (SC) correlations for A533B class I steel.

Figure 5.8 K_{Id} and σ_{yd} versus temperature for full speed
5.26 m/s (207 in/s) Charpy impact tests on
A533B steel after Glover, Johnson, and Radon[50].

also rather high upper end magnitudes. The dynamic fracture toughness, K_{Id}, can be determined through a similar correlation developed by Sailors and Corten.[22] Again, the virgin AR material predictions agree with published data. A comparison with the data of Glover, Johnson, and Radon[50] gives some confidence to the correlation. (See Figures 5.7 and 5.8). The similarity between K_{Ic} and K_{Id} correlations leads to the same trend observed above between the AR and fatigued conditions. The simple relationships in the transition region are limited to correlating K_{Ic} or K_{Ic} values and Charpy test results at the same temperature. The two-step correlation proposed by Barsom[39] involving a temperature shift and a K_{Id}-CVN correlation for the transition region was useless due to scatter in data points and an overconservative temperature shift.

5.7 CVN-K_{Ic} Correlation Limits

It is very difficult to predict the fracture toughness of materials because of the inability to duplicate complex operational conditions precisely. Despite uncompromising criticism, much effort has been applied toward correlating simple CVN to fracture toughness, K_{Ic}. The most obvious limitation to the correlations, and perhaps the most difficult to overcome, is the difference of notch acuity between an actual fatigue crack and the blunt notch of a Charpy specimen. The analysis performed by Ritchie[41] suggests that fracture toughness measurements be twofold, that is, to base conclusions on Charpy impact data as well as on fracture toughness data. His results clearly exemplify the

possible paradox of increasing CVN energy coinciding with decreasing toughness (See Figure 5.9). The effects of fatigue upon the mechanical properties and microstructure here, should be virtually the same as that reported by Riedy[47]. He found that 10^4 cycles of elastic fatigue caused the creation of mobile dislocations and rapid strain propagation. An increase in the dislocation density and the formation of dislocation subcells from tangles were also observed. The subcells may attribute to the increase in CVN energy by providing a decreasing grain size effect. That is to say that the subcells may plastically flow and cleave in a similar manner to a finer grain structure. It is therefore possible for the paradox to occur in this particular situation where the microstructural observations justify the necessity for continued research.
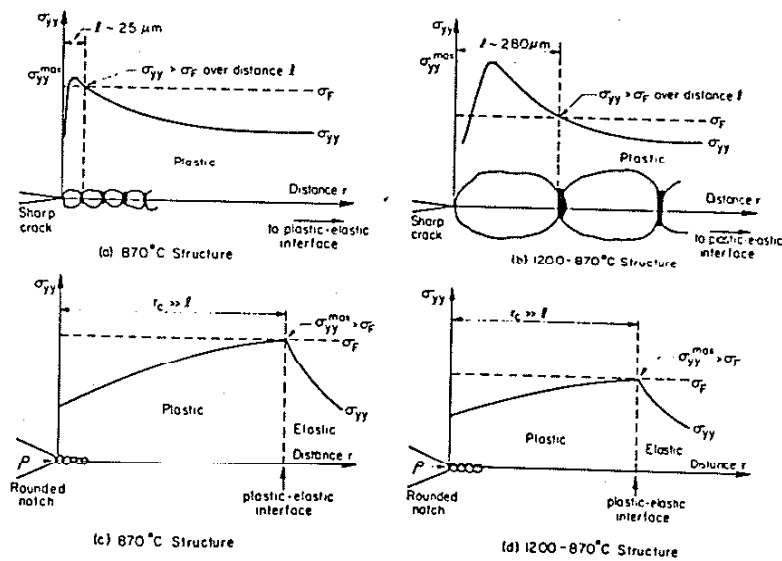
Figure 5.9 Model of apparent CVN-K_{Ic} correlation paradox:
(a) the fine grain size has a shorter characteristic distance ℓ than (b) a course grain size ahead of a sharp crack, and consequently exhibits a lower fracture toughness. Ahead of a blunt notch the fracture stress is greater for the fine grain structure (c) than the course grain structure (d) and thus the fracture toughness here is greater for the fine grain structure (41).

6.0 CONCLUSIONS

From the studies of the effects of fatigue in the elastic regime on the impact behavior of low to medium and medium to high strength steel, where brittle and ductile test temperatures were selected, a distinguishable result was revealed. The fatigue affected the Charpy impact properties of SAE 1018, A533B Class I, and A553B Class I HT steels by decreasing each respective NDT and DBTT to significantly lower temperatures regimes. The A533B Class II steel, which possessed the greatest strength and ductility, displayed no notable changes in impact characteristics following fatigue and incremental plastic strain tests. Comparison between brittle and ductile postfatigue impact results revealed that virtually identical impact toughness increases occurred independently of fatigue temperature.

Low cycle elastic fatigue may be desirable by reason that the lifetime of operational structures may be enhanced. This theory is in agreement with prior investigations that have shown that cycling below the fatigue limit can actually strengthen some steels so that subsequent over those predicted for virgin materials.

The present study revealed that the relatively small size Charpy specimens might be used to obtain fracture toughness data through instrumented Charpy tests. The correlations between CVN and K_{Ic} predict increased toughness resulting from fatigue but due to the empirical nature of the relations the toughness predictions are dependent upon specific material impact parameters and therefore require additional data bases for comparison.

The microstructure developed during fatigue is critical in the fracture process and necessitates the observation of variable notch acuity. Steels of varying microstructure present the paradox of decreasing fracture toughness with concurrent increases in impact toughness. Toughness evaluation in such steels must include an assessment of resistance to fracture ahead of both sharp cracks and rounded notches.

APPENDIX

This appendix presents a method, described by Ireland[46], for comparison between the recorded energy trace and the measured dial reading for instrumental Charpy V-Notch impact testing. The maximum energy E_0 obtainable by the hammer or instrumented tup assembly (before impact with the specimen) can be found from

$$E_0 = \frac{1}{2} I \, v_0^2 \qquad (A1)$$

where v_0 is the hammer velocity immediately prior to impact and I is the moment of inertia of the assembly given by

$$I = \frac{\rho_w}{g} \qquad (A2)$$

where ρ_w is the effective hammer weight and g is the acceleration due to gravity. For the case at hand, a 264 ft·lb capacity Tinius Olsen pendulum type test stand was used ($E_0 = 264$ ft·lb.).

When the tup makes contact with a test specimen, the hammer energy is reduced by an amount ΔE_0 given as

$$\Delta E_0 = E_I + E_{SD} + D_B + E_{MV} + E_{ME} \qquad (A3)$$

where

E_I = increment of energy required to accelerate the specimen from rest to the velocity of the hammer,

E_{SD} = total energy consumed by bending the specimen,

E_B = energy consumed by Brinell-type deformation at the specimen load points,

E_{MV} = energy absorbed by the impact machine through vibrations, and

E_{ME} = stored elastic energy absorbed by the machine at the specimen load points.

For simplicity it is reasonable to assume that E_I, E_B, E_{MV}, and E_{ME} are negligible such that

$$\Delta E_0 = E_{SD} = E_0 - E_f \tag{A4}$$

where E_f is the kinetic energy at time τ after initial contact between specimen and tup. E_f may be expressed in terms of hammer velocity at time τ like E_0 was in Eq. A1, so Eq. A4 reduces to

$$\Delta E_0 = \frac{1}{2} I (v_0^2 - v_f^2) \tag{A5}$$

Now since the relationship of force equals the product of mass and acceleration, the area under the force-time curve can be written as

$$\int_0^\tau P dt + I(v_0 - v_f) \tag{A6}$$

where P is the force, t is the time, and τ is the elapsed time after initial contact between specimen and tup. Equations A5 and A6 can be combined to yield

$$\Delta E_0 = E_a (a - \frac{E_a}{4E_0})$$
(A7)

where, by definition

$$E_a = \nu_0 \int_0^\tau Pdt$$
(A8)

The aforementioned instrumentation system provides E_a directly from the energy-time signal. Now the energy consumed in bending the specimen can be found directly from Eq. A8. Table A1 portrays the comparison between dial readings and recorded energy signals.

Table A1   Dial Reading Comparison with Calculated Values

Material	Specimen Number	Pre-fatigue Condition	Fracture Temperature (°C)	Dial Energy Reading (ft·lb)	ΔE_0 (ft·lb)	E_a (ft·lb)
A533B II	89	IPST	-40	168	159	195
A533B II	105	10^4 @ RT	-10	160	149	180
A533B I	12	10^4 @ RT	-75	123	114	130
A533B I HT	1	10^4 @ 100°C	RT	123	115.5	132
A533B I HT	16	10^4 @ RT	55	147	136	160
SAE 1018	8	AR	77	95	91	100

IPST = incremental plastic strain test

RT = room temperature

AR = as received

E_a = energy from energy-time signal

ΔE_0 = the calculated energy

REFERENCES

1. R. W. Hertzberg, Deformation and Fracture Mechanics of Engineering Materials, John Wiley and Sons, New York, pp. 45-48, (1976).

2. A. S. Eldin and S. C. Collins, "Fracture and Yield Stress of 1020 Steel at Low Temperatures," Journal of Applied Physics, 22, 1296, (1951).

3. E. T. Wessel, "A Tensile Study of Brittle Behavior of a Rimmed Structural Steel," ASTM Proceedings, Vol. 56, pp. 540-552, (1956).

4. J. F. Knott and A. H. Cottrell, "Notch Brittleness in Mild Steel," Journal of the Iron and Steel Institute, pp. 249-260, (March 1963).

5. D. A. Curry, "Cleavage Micromechanisms of Crack Extension in Steels," Metal Science, pp. 319-326, (August-September 1980).

6. A. H. Cottrell, "Theory of Brittle Fracture in Steel and Similar Metals," Transactions of the Metallurgical Society of AIME, pp. 192-203, (April 1958).

7. G. R. Odette and G. E. Lucas, "Analysis of Cleavage Fracture Potential of Martensitic Stainless Steel Fusion Structures," Journal of Nuclear Materials, Vol. 117, pp. 264-286, (1983).

8. T. C. Lindley, "The Effect of Precipitate Size on the Cleavage Fracture Characteristics of an Iron-Carbon Alloy," Journal of the Iron and Steel Institute, pp. 984-987, (July 1969).

9. D. A. Curry and J. F. Knott, "The Relationship Between Fracture Toughness and Microstructure in the Cleavage Fracture of Mild Steel," Metal Science, pp. 1-6, (January 1976).

10. G. Oates, "Effect of Hydrostatic Stress on Cleavage Fracture in a Mild Steel and a Low-Carbon Manganese Steel," Journal of the Iron and Steel Institute, pp. 930-935, (Sept. 1968).

11. D. A. Curry and J. F. Knott, "Effects of Microstructure on Cleavage Fracture Stress in Steel," Metal Science, pp. 511-514, (Nov. 1978).

12. D. A. Curry and J. F. Knott, "Effect of Microstructure on Cleavage Fracture Toughness of Quenched and Tempered Steels," Metal Science, pp. 341-345, (June 1979).

13. F. Smith, "Physical Basis of Yield and Fracture," Conference Proceedings of the Institute of Physics and Physics Society, p. 36, (1966).

14. D. Broek, "Some Considerations on Slow Crack Growth," _International Journal of Fracture Mechanics_, Vol. 4, pp. 19-34, (March 1968).

15. R. O. Ritchie, J. F. Knott, and J. R. Rice, "On the Relationship Between Critical Tensile Stress and Fracture Toughness in Mild Steel," _Journal of the Mechanics and Physics of Solids_, Vol. 21, pp. 395-410, (1973).

16. J. F. Knott, "Micromechanisms of Fibrous Crack Extension in Engineering Alloys," _Metal Science_, pp. 327-336, (Aug.-Sept. 1980).

17. R. M. Thomson and J. E. Sinclair, "Mechanics of Cracks Screened by Dislocations," _Acta Metallurgica_, Vol. 30, pp. 1325-1334, (1982).

18. J. P. Tanaka, C. A. Pampillo, and J. R. Low, Jr., "Fractographic Analysis of the Low Energy Fracture of an Aluminum Alloy," _Review of Developments in Plane Strain Fracture Toughness Testing_, ASTM STP 463, American Society for Testing and Materials, pp. 191-215, (1970).

19. F. A. McClintock, "Local Criteria for Ductile Fracture," _International Journal of Fracture Mechanics_, Vol. 4, pp. 101-130, (June 1968).

20. C. D. Beachom, "The Effects of Crack Tip Plastic Flow Directions Upon Microscopic Dimple Shapes," _Metallurgical Transactions A_, Vol. 6A, pp. 377-383, (Feb. 1975).

21. J. M. Barsom and S. T. Rolfe, "Correlations Between K_{Ic} and Charpy V-Notch Test Results in the Transition-Temperature Range," _Impact Testing of Metals_, ASTM STP 466, American Society for Testing and Materials, pp. 281-302, (1970).

22. R. H. Sailors and H. T. Corten, "Relationship Between Material Fracture Toughness Using Fracture Mechanics and Transition Temperature Tests," _Fracture Toughness, Proceedings of the 1971 National Symposium on Fracture Mechanics, Part II_, ASTM STP 514, American Society for Testing and Materials, pp. 164-191, (1972).

23. T. J. Koppenaal, "Dynamic Fracture Toughness Measurements of High-Strength Steels Using Precracked Charpy Specimens," _Instrumented Impact Testing_, ASTM STP 563, pp. 92-117, (1974).

24. G. T. Hahn and A. R. Rosenfield, "Sources of Fracture Toughness: The Relation Between K_{Ic} and the Ordinary Tensile Properties of Metals," _Applications Related Phenomena in Titanium Alloys_, ASTM STP 432, pp. 5-32, (1968).

25. J. M. Krafft, "Correlation of Plane Strain Crack Toughness with Strain Hardening Characteristics of a Low, a Medium, and a High-Strength Steel," _Applied Materials Research_, Vol. 3, p. 88, (1963).

26. J. M. Krafft and G. R. Irwin, "Crack Velocity Considerations," _Fracture Toughness and Its Applications,_ ASTM STP 381, p. 84, (1965).

27. F. J. Lauta and E. A. Steigerwald, "Influence of Work Hardening Coefficient on Crack Propagation in High-Strength Steels," _AFML-TR-65-31,_ Air Force Materials Laboratory, (May 1965).

28. G. T. Hahn and A. R. Rosenfield, "Metallurgical Factors Affecting Fracture Toughness of Aluminum Alloys," _Metallurgical Transactions A,_ Vol. 6A, pp. 653-668, (April 1975).

29. J. R. Rice and M. A. Johnson, "Inelastic Behavior of Solids," M. F. Kanninen, et al., eds., p. 641, McGraw-Hill, New York, (1970).

30. J. W. Hutchinson, _Journal of the Mechanics and Physics of Solids,_ Vol. 16, p. 13, (1968).

31. N. Levy, P. V. Marcal, W. J. Ostergren, and J. R. Rice, _International Journal of Fracture Mechanics,_ Vol. 7, p. 143, (1971).

32. A. J. Birkle, R. P. Wei, and G. E. Pellisier, Trans. ASM, Vol. 59, p. 981, (1966).

33. J. H. Mulherin and H. Rosenthal, _Metallurgical Transactions,_ Vol. 2, p. 427, (1971).

34. J. R. Low, Jr., R. H. Van Stone, and R. H. Merchant, "NASA Technical Report No. 2," _Research Grant NGR 38-087-003,_ Carnegie-Mellon University, (1972).

35. J. J. Hauser and M. G. Wells, _Technical Report AFML-TR-69-339,_ Wright Patterson AFB, Ohio, (1969).

36. T. B. Cox and J. R. Low, Jr., "NASA Technical Report No. 4," _Research Grant NGR-39-087-003,_ Carnegie-Mellon University, (1972).

37. D. S. Thompson and S. A. Levy, _AFML-TR-70-171,_ Wright Patterson AFB, Ohio, (1970).

38. R. Roberts and C. Newton, "Interpretive Report on Small-Scale Test Correlations with K_{Ic} Data," _WRC Bulletin 265,_ (1981).

39. J. M. Barsom, "Development of the AASHTO Fracture Toughness Requirements for Bridge Steels," _Engineering Fracture Mechanics,_ 7, pp. 605-618, (1975).

40. J. R. Hawthorne and T. R. Mager, "Relationship Between Charpy V and Toughness Using Fracture Mechanics K_{Ic} Assessments of A533B Class 2 Pressure Vessel Steel," _Fracture Toughness, Proceedings of the 1971 National Symposium on Fracture Mechanics,_ Part II, ASTM STP 513, pp. 151-163, (1972).

41. R. O. Ritchie, "On the Relationship Between Fracture Toughness and Charpy V-Notch Energy in Ultrahigh Strength Steel," What Does the Charpy Test Really Tell Us, pp. 54-73, Wiley, New York, (1979).

42. R. O. Ritchie, B. Francis, and W. L. Server, Metallurgical Transactions A., Vol. 7A, p. 831, (1976).

43. J. P. Naylor and R. Blondeau, Metallurgical Transactions A., Vol. 7A, p. 891, (1976).

44. T. Tom, Report No. LBL-1856, Lawrence Berkeley Laboratory, University of California. (Sept. 1973).

45. ASTM Annual Standards, "Standard Methods and Definitions for Mechanical Testing of Steel Products," ASTM Annual Standards, A370 Sec. 18-23, pp. 36-39, (1982).

46. D. R. Ireland, "Procedures and Problems Associated with Reliable Control of the Instrumented Impact Test," Instrumented Impact Testing, ASTM STP 463, American Society for Testing and Materials, pp. 3-29, (1974).

47. A. W. Riedy and J. F. Stubbins, "Effects of Fatigue in the Elastic Regime on the Mechanical Properties of Low Carbon Steels," UILU-ENG 83-3605, FCP Report No. 49, (1983).

48. T. R. Mayer and F. O. Thomas, "Evaluation by Linear Elastic Fracture Mechanics of Radiation Damage to Pressure Vessel Steels," Westinghouse Atomic Power Divisions, WCAP-7328, HSST Technical Reports, (Nov. 1969).

49. W. O. Shabbits, W. H. Pryle, and E. T. Wessel, "Heavy Section Fraction Toughness Properties of A533 Grade B Class I Steel Plate and Submerged Arc Weldments," Westinghouse Atomic Power Divisions, WCAP-7414. HSST Technical Report 6, (Dec. 1969).

50. A. P. Glover, F. A. Johnson, and J. C. Radon, "Dynamic-fracture Toughness of A533B Steel," Experimental Mechanics, pp. 172-178, (May 1977).